DØ Note XXXX
March 7, 2005
Version 1.3

Measurement of the Drell-Yan Differential Cross Section and Forward-Backward Asymmetry in $p\bar{p} \rightarrow e^+e^-$ Events using the DØ Detector

John Ellison, Raymond Gelhaus, and Ia Iashvili

University of California, Riverside

We present measurements of the inclusive Drell-Yan e^+e^- differential cross section ($d\sigma/dM_{e^+e^-}$) and forward-backward asymmetry (A_{FB}) as a function of the dielectron invariant mass over the range $50 - 400$ GeV/c^2. The data sample consists of 177.3 pb^{-1} of $p\bar{p}$ collisions at $\sqrt{s} = 1.96$ TeV collected by the DØ detector. The results are consistent with the predictions of the standard model.

Contents

I. INTRODUCTION

The Drell-Yan process describes the annihilation of a quark-antiquark pair and the production of a dilepton pair via an intermediate Z-boson or virtual photon $p\bar{p} \rightarrow \gamma^*/Z \rightarrow e^+e^-$ [1]. In this analysis we look at the e^+e^- final state. The presence of both vector and axial-vector couplings of the quarks and leptons to the Z-boson gives rise to an asymmetry in the polar emission angle θ of the electron in the rest frame of the e^+e^- pair. The differential cross section for the parton level process $q\bar{q} \rightarrow \gamma^*/Z \rightarrow e^+e^-$ can be written

$$\frac{d\sigma}{d(\cos\theta)} = A(1+\cos^2\theta) + B\cos\theta, \tag{1}$$

The weak interaction introduces the asymmetry ($B \neq 0$), and A and B are functions that depend on the weak isospin and charge of the incoming quarks and the e^+e^- invariant mass. To minimize the effect of the unknown transverse momenta of the incoming quarks we use the Collins-Soper reference frame [2]. The particle four-vectors are transformed to the e^+e^- rest frame and the polar angle θ^* is measured with respect to the z-axis, defined as the bisector of the proton beam momentum vector $\mathbf{P}_1$ and the negative antiproton beam momentum vector $-\mathbf{P}_2$, as shown in Fig. 1. The y-axis is parallel to $\mathbf{P_1} \times \mathbf{P_2}$, and $\cos\theta^*$ is given by [2]

$$\cos\theta^* = 2Q^{-1}(Q^2+Q_T^2)^{-1/2}(l^+\bar{l}^- - l^-\bar{l}^+) \tag{2}$$

where l^ν is the electron four-momentum in the lab frame, $\bar{l}^\nu$ is the positron four-momentum in the lab frame, $Q^\nu = l^\nu + \bar{l}^\nu$ is the dielectron four-momentum in the lab frame, and $l^\pm = 2^{-1/2}(E_l \pm p_{zl})$.

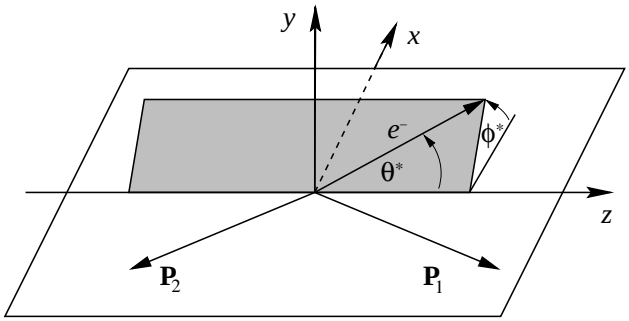

FIG. 1: The Collins-Soper reference frame. The angle θ^* is measured with respect to the z-axis defined as the bisector of the proton beam momentum $\mathbf{P}_1$ and the negative of the antiproton beam momentum $-\mathbf{P}_2$. $\mathbf{P}_1$ and $\mathbf{P}_2$ are measured in the e^+e^- rest frame.

The forward-backward asymmetry A_{FB} is defined by

$$A_{FB} = \frac{\sigma_F - \sigma_B}{\sigma_F + \sigma_B} \tag{3}$$

where σ_F and σ_B are the forward and backward cross sections defined by

$$\sigma_F = \int_0^1 \frac{d\sigma}{d(\cos\theta^*)} d(\cos\theta^*) \tag{4}$$

$$\sigma_B = \int_{-1}^0 \frac{d\sigma}{d(\cos\theta^*)} d(\cos\theta^*) \tag{5}$$

The forward-backward asymmetry depends on the vector and axial-vector couplings of the quarks and leptons to the Z-boson and is therefore sensitive to the effective weak mixing angle $\sin^2\bar{\theta}_W$. The largest asymmetry occurs at center-of-mass energies of around 70 GeV and above 110 GeV. At the Z-pole the asymmetry is dominated by the couplings of the Z boson and arises from the interference of the vector and axial components of its coupling. At large invariant mass the asymmetry is dominated by γ^*/Z interference and is almost constant (≈ 0.6), independent of invariant mass. The Tevatron allows measurement of the forward-backward asymmetry at partonic center-of-mass energies above the center-of-mass energy of LEP II. This measurement can be used not only to confirm the standard model γ^*/Z interference which dominates in this region, but also to investigate possible new phenomena which may alter A_{FB} such as new neutral gauge bosons [3] or large extra dimensions [4]. This analysis is directed at testing the standard model predictions of the forward-backward asymmetry over the invariant mass range $50 - 400$ GeV.

II. MONTE CARLO SIMULATION

Monte Carlo Drell-Yan events are used in this analysis for the calculation of the unfolding correction and comparison to data. The Monte Carlo events are generated using PYTHIA/PHOTOS with the CTEQ6M parton distribution functions (PDFs). PHOTOS[6] has been implemented into PYTHIA[5], because PHOTOS gives a better description of the final state QED corrections, which are necessary for this analysis, than standard PYTHIA. The events are then processed through the p14.05.02 PMCS fast Monte Carlo simulation, and p15.06.01 wz_epmcs package to simulate the kinematic and geometric acceptance, and the response of the detector. Photons that have their momenta within $\Delta R = 0.2$ of the direction of an electron are merged with the electron; i.e. the photon 4-vector is added to that of the electron. The 0.2 cone size roughly corresponds to the extent of the EM lustering algorithm used in the calorimeter. If $\Delta R(e - \gamma) > 0.2$ the photon 4-vector is separate and treated as part of the recoil system. In order to obtain a sufficient number of events at high dielectron invariant masses, the events are generated in several mass ranges. The invariant mass ranges, cross sections, and total number of events are given in Table I. The total number of events generated in all mass ranges is 1,725,000.

Mass Region (GeV/c^2)	Avg. Cross Section (pb)	Pythia/Photos Events	No FSR Events
$40 < M_{ee} < 75$	26.49	450000	450000
$75 < M_{ee} < 110$	191.7	450000	450000
$110 < M_{ee} < 200$	3.523	375000	375000
$200 < M_{ee} < 500$	0.3029	225000	225000
$500 < M_{ee} < 1000$	0.004659	225000	225000

TABLE I: Drell-Yan Monte Carlo samples.

Monte Carlo samples generated with PYTHIA using CTEQ6M, but without QED final state radiation (FSR) are used in obtaining the unfolding correction factor (see Section IX). Table I gives the invariant mass ranges, cross sections, and total number of events for the no-FSR sample. The total number of events generated for this sample in all mass ranges is 1,725,000.

In the PMCS detector simulation the reconstructed energy E of electrons is related to the generated electron energy E_0 by

$$E = \alpha E_0 + \delta \tag{6}$$

where α is the electron energy scale and δ is the energy offset. The EM resolution is parametrized by

$$\frac{\Delta E}{E} = \sqrt{C^2 + S^2 + N^2/E^2} \tag{7}$$

The sampling term S and noise term N are taken from test beam data; $S = 0.15$ GeV/c^2, and $N = 0.29$ GeV for the central calorimeter. The electron energy scale, energy offset, and electron resolution constant term are optimized for the PYTHIA/PHOTOS Drell-Yan Monte Carlo sample by tuning the Monte Carlo to data, using the methods described in [7]. The following values are found to give best agreement with the data:

$\alpha_{CC} = 1.006 \pm 0.003$

$\delta_{CC} = 0.069 \pm 0.045$

$C_{CC} = 0.045 \pm 0.002$

Figure 2 shows the $-$log likelihood fit for the electron energy scale in the CC region. The $-$log likelihood fits for energy offset and constant term in the CC region are shown in Fig. 3 and Fig. 4, respectively.

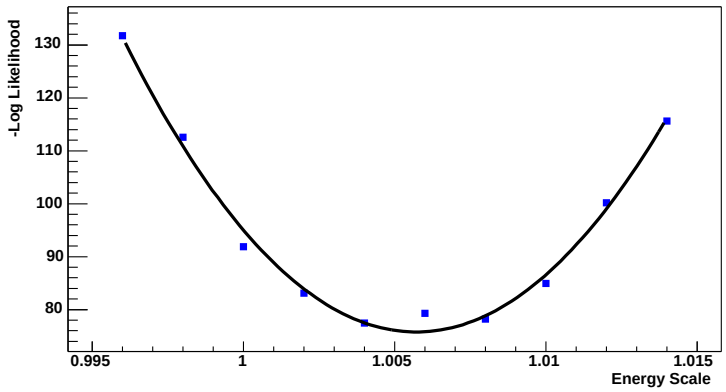

FIG. 2: −Log likelihood vs. electron energy scale in the CC region.

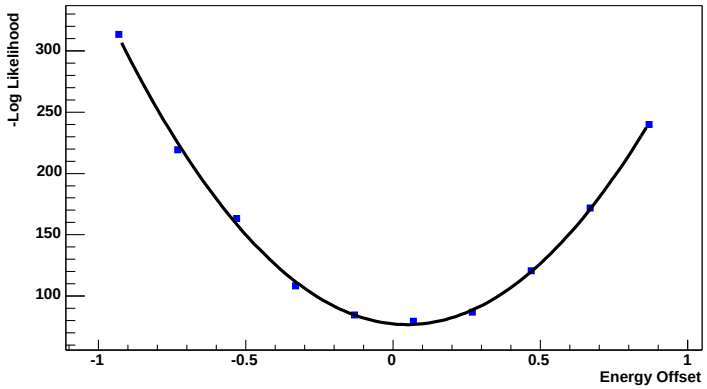

FIG. 3: −Log likelihood vs. electron energy offset in the CC region.

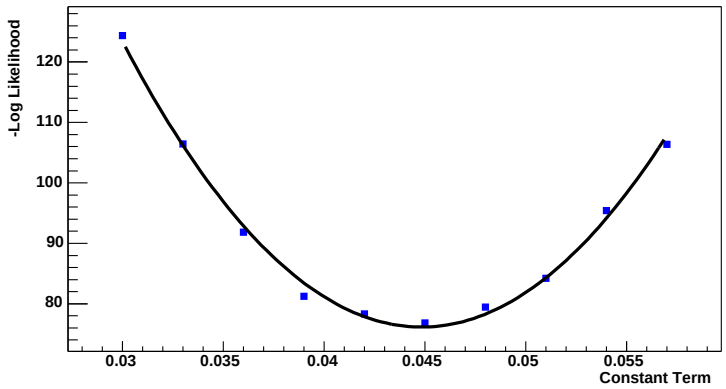

FIG. 4: −Log likelihood vs. electron energy constant term in the CC region.

III. DATA SET AND TRIGGER

The initial skimmed data set required at least one EM object with id $= 10, \pm 11$ and $E_T > 15$ GeV (CSskim-1EMloose). There was no initial trigger requirement. The data was reconstructed using d0reco versions p14.03.00, p14.03.01, p14.03.02, p14.05.00, p14.05.02, and p14.06.00. All corrections were made using the packages wz_analyze v01-00-12 and d0correct v00-00-06. Bad CALO, SMT, and CFT runs, as well as runs/lumi blocks declared BAD by the Jet/MET group were removed from the sample. Furthermore, data corresponding to luminosity blocks that can not be normalized is not used in the analysis. The total luminosity of this sample is 177 ± 12 pb^{-1}.

Events are required to pass one of the following trigger combinations (given in order of preference) depending on which triggers were unprescaled in a given run:

- E1_SH30 or E1_SHT20 or E2_SHT20 or E3_SHT20
- E1_SH30 or E1_SHT20 or E2_SHT20
- E1_SH30 or E1_SHT20
- E1_SHT20
- EM_HI_SH or EM_HI_2EM5_SH
- EM_HI_SH
- EM_HI
- EM_MX_SH
- EM_MX

The first four bullets correspond to global trigger list CMT12 (runs $\geq$ 178722), and the rest correspond to CMT8-11 (runs $\leq$ 178721). Table II breaks down each trigger requirement.

The efficiency of the single electron trigger combination was calculated with the "tag/probe" method using the em_cert package. First, two good EM clusters are selected with the following criteria:

- ID $= 10$ or ± 11
- $E_T > 15$ GeV
- EM Fraction > 0.9
- Isolation < 0.15
- CC: HMx7 $< 12 + slope \times (E_T - 45$ GeV), where $slope = 0.020$ GeV^{-1}
- `in_fiducial`: $\phi > 0.02$ radians from module boundary in CC; $|z| < 115$ cm in the CC
- $|\eta_{det}| < 1.1$
- Removed bad calorimeter cells[14]

Trigger Name	L1	L2	L3
E1_SH30	CEM(1,11)	none	ELE_NLV_SH(1,30)
E1_SHT20	CEM(1,11)	none	ELE_NLV_SHT(1,20)
E2_SHT20	CEM(2,6)	none	ELE_NLV_SHT(1,20)
E3_SHT20	CEM(1,9)CEM(2,3)	none	ELE_NLV_SHT(1,20)
EM_HI_SH	CEM(1,10)	EM(1,12)	ELE_LOOSE_SH_T(1,20)
EM_HI_2EM5_SH	CEM(2,5)	EM(1,12)	ELE_LOOSE_SH_T(1,20)
EM_HI	CEM(1,10)	EM(1,12)	ELE_LOOSE(1,30)
EM_MX_SH	CEM(1,15)	none	ELE_LOOSE_SH_T(1,20)
EM_MX	CEM(1,15)	none	ELE_LOOSE(1,30)
	L1 triggers		
CEM(1,9)CEM(2,3)	one EM trigger tower with $E_T > 9$ GeV another EM trigger tower with $E_T > 3$ GeV		
CEM(1,10)	one EM trigger tower with $E_T > 10$ GeV		
CEM(1,11)	one EM trigger tower with $E_T > 11$ GeV		
CEM(1,15)	one EM trigger tower with $E_T > 15$ GeV		
CEM(2,5)	two EM trigger towers with $E_T > 5$ GeV		
CEM(2,6)	two EM trigger towers with $E_T > 6$ GeV		
	L2 triggers		
EM(1,12)	one EM candidate with $E_T > 12$ GeV (not present for runs < 169524)		
	L3 triggers		
ELE_LOOSE(1,30)	one loose electron is found satisfying $E_T > 30$ GeV and $\|\eta\| < 3$		
ELE_LOOSE_SH_T(1,20)	one loose electron is found satisfying transverse shower shape requirements, $E_T > 20$ GeV, and $\|\eta\| < 3$		
ELE_NLV_SH(1,30)	one loose electron is found satisfying loose shower shape requirements, $E_T > 30$ GeV, and $\|\eta\| < 3.6$		
ELE_NLV_SHT(1,20)	one loose electron is found satisfying tight shower shape requirements, $E_T > 20$ GeV, and $\|\eta\| < 3.6$		

TABLE II: SingleEM triggers.

The "tag" or highest E_T electron is a tight cut electron (has a track match and $E_T > 25$ GeV/c) and must pass the level 1, 2, and 3 requirements for the EM_HI_SH, EM_HI_2EM5_SH, E1_SHT20, or E2_SHT20 tight triggers. The "probe" or second highest E_T electron must pass the level 1, 2, and 3 requirements of the combined trigger above. The trigger efficiency versus electron E_T is shown in Fig. 5. The data are fit using an error function. The uncertainties in the efficiencies are calculated using the program described in Ref. [11].

A Monte Carlo Drell-Yan sample is used to determine if the trigger efficiency has a mass dependence. The overall event trigger efficiency is calculated using the same Monte Carlo sample used for the unfolding correction calculation (see Section IX). Using the same cuts

as applied in the unfolding correction calculation, the individual electron trigger efficiency is calculated using the parametrized electron trigger efficiency versus E_T. If either electron passes the trigger requirement, then the event is retained. We calculate the event trigger efficiency versus M_{ee} by dividing the number of events retained by the total number of reconstructed events passing the acceptance cuts ($E_T > 25$ GeV, `in_fiducial`, $|\eta_{det}| < 1.1$). The event trigger efficiency versus M_{ee} is shown in Fig. 6. For the cross section calculation, we use the constant number from the straight line fit with an asymmetric error, $\epsilon_{trig}^{CC-CC} = 1.0000^{+0.0000}_{-0.0002}(\text{stat.})^{+0.0000}_{-0.0006}(\text{sys.})$. The trigger efficiency systematic error is taken from the WZ to electrons cross section measurement [14].

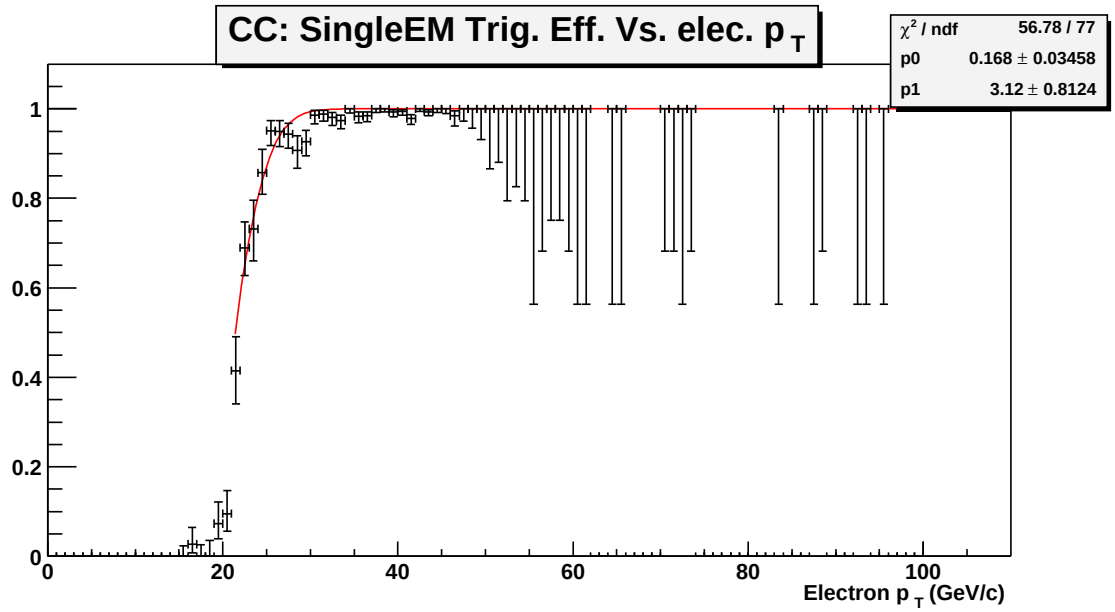

FIG. 5: Single electron trigger efficiency vs. E_T.

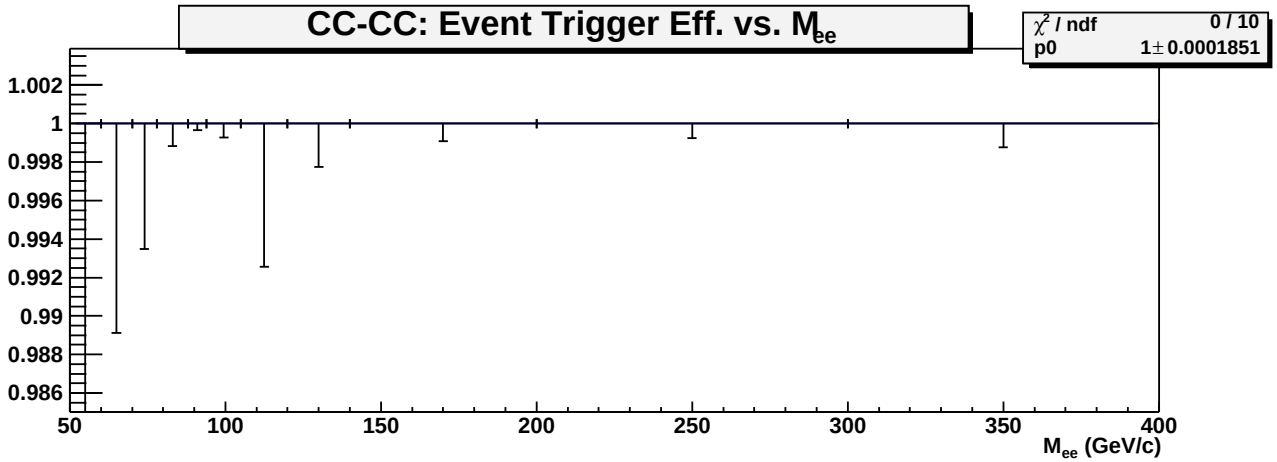

FIG. 6: Event trigger efficiency vs. M_{ee}.

IV. ELECTRON IDENTIFICATION AND EVENT SELECTION

Selected events must have at least two EM objects. To make sure that the EM objects closely resemble an electron the following criteria were applied:

- "Loose" electron:
  - ID = 10 or ±11
  - EM Fraction > 0.9
  - Isolation < 0.15
  - CC: HMx7 $< 12 + slope \times (E_T - 45)$, where $slope = 0.020$ GeV^{-1}
    The H-Matrix χ^2 tends to slightly increase with electron energy, so a E_T-weighted cut is included to ensure the same efficiency for electrons over the full energy range (see Section V).
- "Tight" electron:
  - All the "loose" electron requirements, plus
  - A track matched to the calorimeter cluster (using E/p)

We require one "tight" and one "loose" electron per event. EM objects in the bad calorimeter cell region are not considered as electron candidates [14]. The "tight" electron is required to get a measurement of the charge of the electron, which is required for the A_{FB} measurement. The electrons are required to be within the detector region $|\eta_{det}| < 1.1$. The electrons must also be in the fiducial region of the detector (`in_fiducial`). This cut removes electron candidates in the phi cracks of the CC ($\phi > 0.02$ radians from the module boundary), and at the cryostat edges ($|z| < 115$ cm in the CC).

The electrons were required to have a transverse energy of $E_T > 25$ GeV. If more than two electrons in an event have these requirements only the two highest E_T electrons are chosen. The invariant mass distribution for the signal selection is shown in Fig. 7.

V. EM IDENTIFICATION EFFICIENCY

Electrons are characterized by the following quality cuts: EM fraction, Isolation, and HMx7. The EM fraction is the fraction of cluster energy measured in the electromagnetic layers of the calorimeter section divided by the total cluster energy (hadronic + EM) deposited in the calorimeter section. Isolation is defined by $I = (E_{\text{cone}} - E_{\text{core}})/E_{\text{core}}$, where E_{cone} in the energy in a cone of radius $R = 0.4$ around the direction of the electron, summed over the entire depth of the calorimeter, and E_{core} is the energy in a cone of $R = 0.2$, summed over the EM calorimeter only. Isolation rejects electron candidates which have nearby energy (e.g. from QCD multijet events). HMx7 is a covariance matrix of 7 observables to take into account simultaneously both the energy observed in a given layer and its correlations with energy deposited in the other layers. This quantity quantifies how closely an electromagnetic cluster resembles a real electron, as predicted by a detailed simulation.

The EM-id efficiencies are calculated using $Z \to ee$ candidate events. The energy of the electrons from the $Z \to ee$ decay will be lower than electrons that come from Drell-Yan events at much higher invariant masses. Therefore, we must look how the EM-id variables

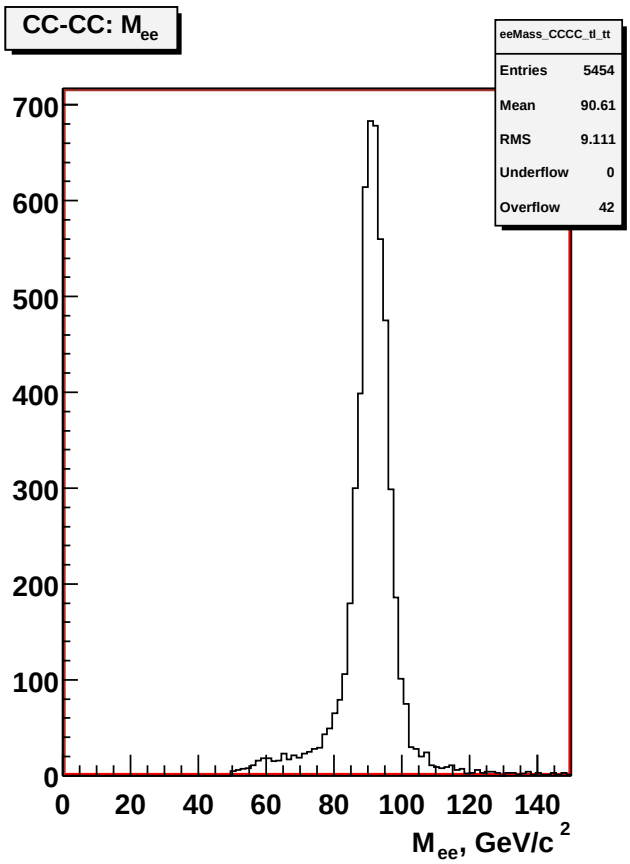

FIG. 7: Distribution of ee invariant mass M_{ee} of the selected data sample.

vary with electron energy. For this study, we use Drell-Yan Monte Carlo events, run through the full detector simulation, that pass our acceptance cuts. Each electron identification variable is plotted versus the electron energy in the CC region. Figure 8 shows that the EM fraction and isolation have no significant energy dependence, but the H-Matrix has a slight energy dependence. The H-Matrix vs. E_T dependence is fit with a straight line shown in Fig. 9. The slope is found to be 0.020 ± 0.001 GeV^{-1} (CC).

For the calculation of EM-id efficiencies, we use the same data sample as is used for the signal selection. The "tag/probe" method is used, where the "probe" electron must have ID $= 10$ or ± 11, `in_fiducial`, in CC region, and $E_T > 25$ GeV. The "tag" electron is a probe electron with all of the electron selection EM-id cuts and a track match. The efficiency is the number of probe electrons passing the cut under study divided by the total number of probe electrons.

$$\epsilon_{cut} = \frac{2(tt) + (tp)}{2(tt) + (tp) + (tf)}, \tag{8}$$

where

tt = number of events where both electrons pass the tag cuts (and therefore pass the cut under study);

tp = number of events where one electron passes the tag cuts and the other passes the cut under study but fails the tag cuts;

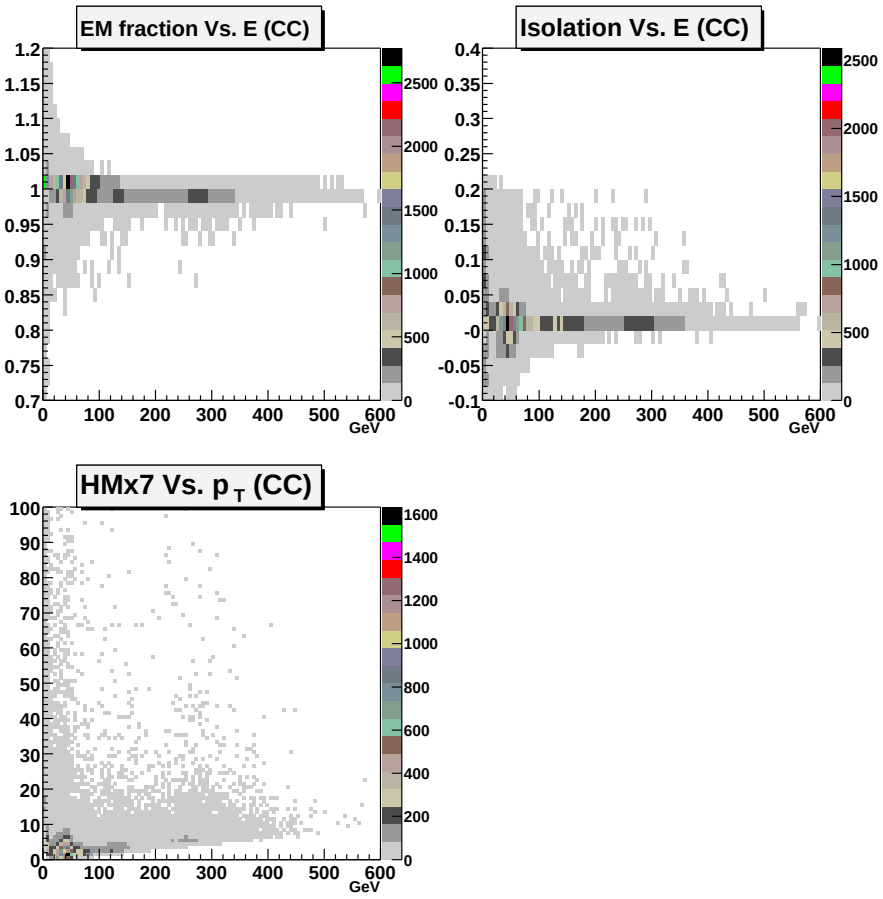

FIG. 8: Monte Carlo EM-id variables vs. electron energy distributions for the CC region.

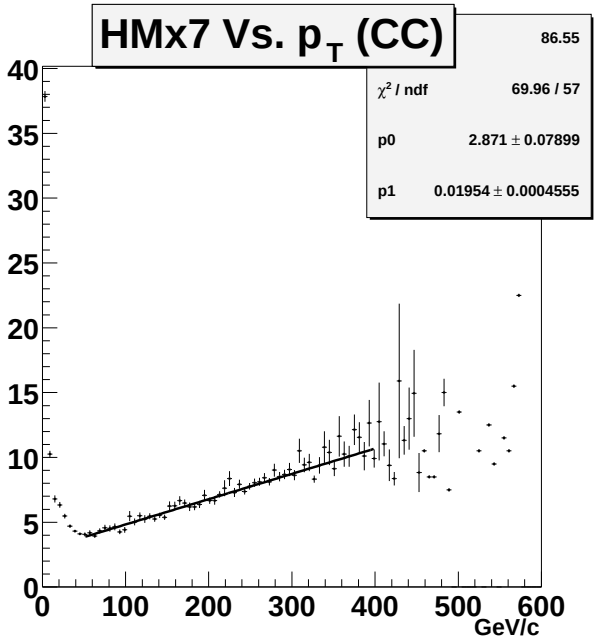

FIG. 9: HMx7 vs. electron E_T distribution for the CC region.

tf = number of events where one electron passes the tag cuts and the other electron fails the cut under study (and therefore fails the tag cuts as well).

The background invariant mass distribution is estimated using four methods [12]:

1. Sideband Technique: Two sidebands on each side of the chosen signal region ($86 < M_{ee} < 96$ GeV) are $60 < M_{ee} < 70$ GeV and $110 < M_{ee} < 120$ GeV. The sidebands are symmetric around the signal region, and span the same invariant mass range. The estimated number of background events is then the average of the two sidebands.

2. Sideband Technique: Similar to Method 1, but with a signal region between $81 < M_{ee} < 101$ GeV. And the estimated number of background events is then the sum of the two sideband regions.

3. Breit-Wigner/Gaussian with Linear Fit: The invariant mass is fit with a Breit-Wigner convoluted with a Gaussian, which accounts for the resolution in the measurement, and a linear background in the region $70 < M_{ee} < 110$ GeV. The signal region is chosen to be $86 < M_{ee} < 96$ GeV. The parameters from the fit are then used to estimate the background.

4. Similar to Method 3, but the signal region is chosen to be $81 < M_{ee} < 101$ GeV.

Methods 3 and 4 are also repeated using an exponential background shape and the EM-id efficiencies found were similar to those found using the linear background. The M_{ee} distributions for the numerator and denominator in Eq. (8) using methods 3 and 4 with the linear background are shown in Fig. 10. The EM-id efficiency is $(91.89 \pm 0.34)\%$ for method one, $(92.51 \pm 0.29)\%$ for method two,$(92.80 \pm 0.32)\%$ for method three, and $(92.57 \pm 0.29)\%$ for method four. Method 4 is used to quote the central value of the efficiency; it is the closest method calculated with the linear background to the average of the four methods. The individual numbers of tt, tp, and tf events integrated over the Z-peak region for method 4 are:

- CC region:

$$tt = 3012.13 \pm 165.30$$
$$tp = 1536.91 \pm 171.76$$
$$tf = 611.28 \pm 120.36$$

The systematic error is determined by subtracting the method that gives the lowest EM-id efficiency by the method that gives the highest EM-id efficiency and then dividing by two. We obtain an EM-id efficiency (ϵ^{CC}_{EM-id}) with total error of $(92.57 \pm 0.54)\%$.

To determine the EM-id efficiency as a function of invariant mass, we model the EM-id efficiency using Monte Carlo, then normalize the distribution to data in the Z-peak region. The efficiency for Monte Carlo events to have two EM objects passing the EM-id requirements is shown separately for forward and backward events in Fig. 11. The decrease in efficiency below and above the Z-pole is due to a combination of bin migration due to detector resolution and photon radiation. Photon radiation can affect the HMx7, isolation, and EM fraction variables, causing the electron to fail the EM-id requirements. The largest effect is on the HMx7 variable. Since the efficiencies for forward and backward events are consistent with one another within the statistical uncertainties, we use the overall EM-id efficiency for all events. Figure 12 shows the Event EM-id efficiency versus invariant mass, which has been normalized to data.

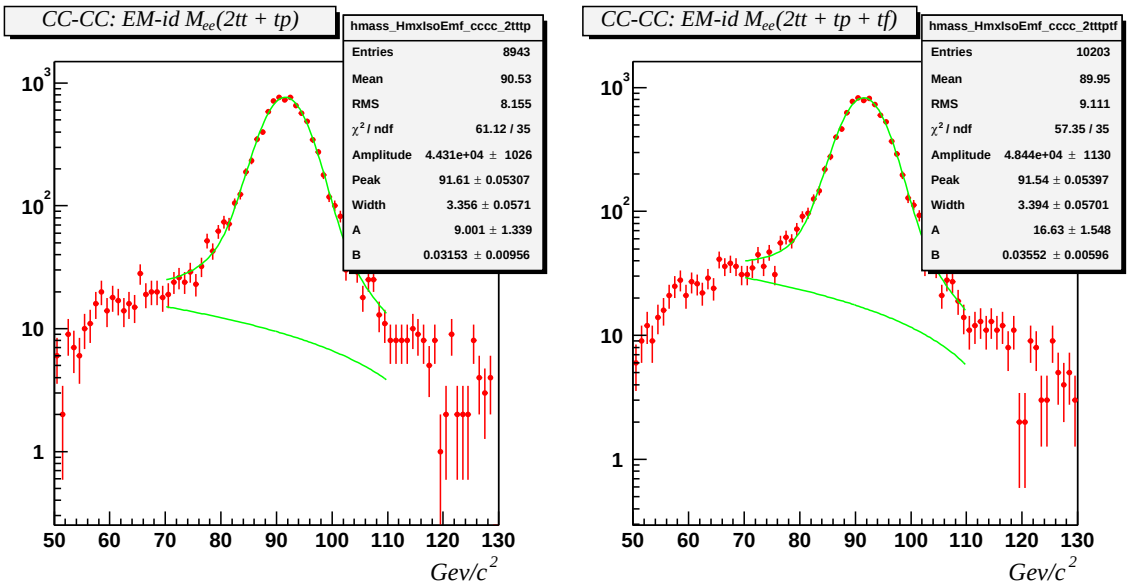

FIG. 10: Invariant mass M_{ee} distributions for the numerator (left) and denominator (right) of Eq. (8) used to determine the EM-id efficiency with background subtraction methods 3 and 4. The points are the data and the lines show the linear background estimate and the result of the fit to a Breit-Wigner convolved with a Gaussian plus a linear background.

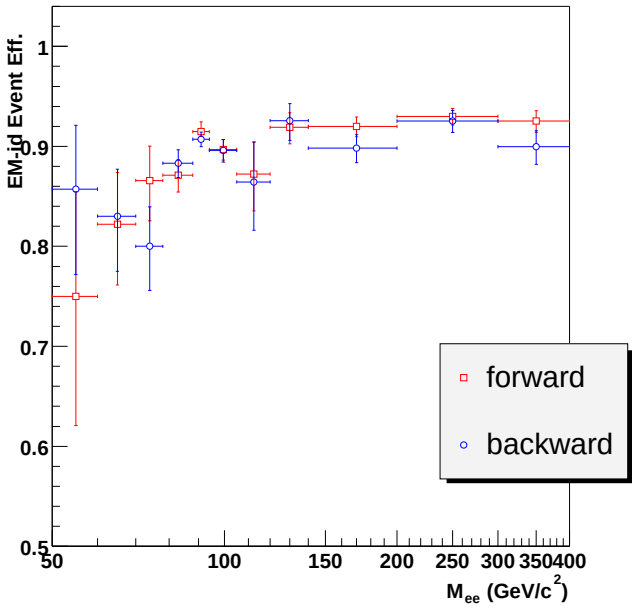

FIG. 11: Efficiency for Monte Carlo events to pass the EM-id requirements vs. M_{ee} for forward and backward events. The efficiencies are not normalized to data.

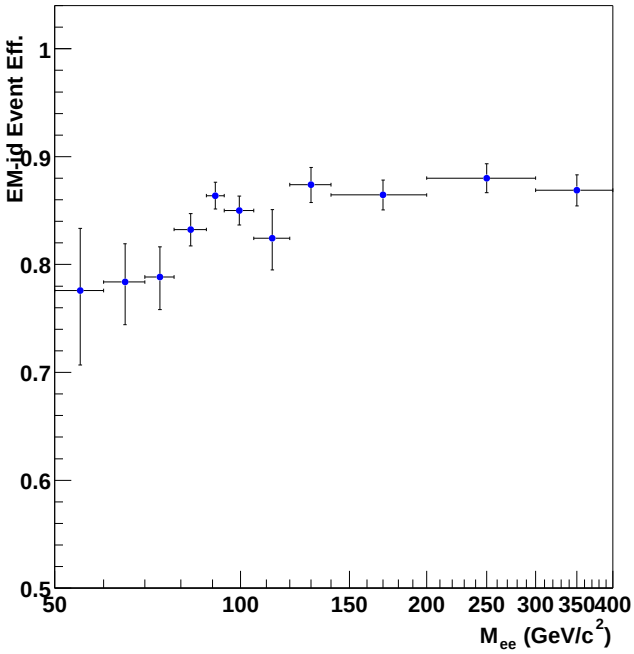

FIG. 12: Event EM-id efficiency vs. M_{ee} for all events. The efficiencies are normalized to data.

VI. TRACK MATCH EFFICIENCY

Requiring an EM cluster to have a matching track helps to remove a large background from QCD multijet production. Isolated EM objects in QCD events are from photons or π^0 mesons, which should not have tracks associated with them. The track match chi-square is defined by

$$\chi^2_{CC} = \left(\frac{\Delta z}{\sigma(z)}\right)^2 + \left(\frac{\Delta\phi}{\sigma(\phi)}\right)^2 + \left(\frac{E_T/p_T - 1}{\sigma(E_T/p_T)}\right)^2 \tag{9}$$

The track match efficiency is calculated using $Z \to ee$ candidate events. The same data sample as was used to calculate the EM-id efficiency is used here. Events should have at least two EM objects. Then the two highest E_T EM objects must pass the "loose" electron cuts. Each "loose" electron is tested to see if it has a matched track. The efficiency is given by:

$$\epsilon_{trk} = \frac{2N_2}{N_1 + 2N_2}, \tag{10}$$

where N_1 is the number of events with one cluster matched to a track, and N_2 is the number of events with both clusters matched to tracks. The backgrounds are calculated using the same four methods as is used for the EM-id efficiency. The M_{ee} distributions for the numerator and denominator in Eq. (10) using methods 3 and 4 with the linear background are shown in Fig. 13. The track-match efficiency is found to be $(79.45 \pm 0.52)\%$ for method one, $(79.40 \pm 0.47)\%$ for method two,$(79.85 \pm 0.52)\%$ for method three, and $(79.68 \pm 0.46)\%$ for method four. Method 4 is used to quote the central value of the efficiency; it is the closest method calculated with the linear background to the average of the four methods. The individual numbers of two-track, one-track and zero-track events, integrated over the Z-peak region are:

- CC region:

  0 Track Match = 126.48 ± 137.95

  1 Track Match (N_1) = 1537.90 ± 171.82

  2 Track Match (N_2) = 3014.09 ± 233.84

The M_{ee} distributions for the numerator and denominator in Eq. (10) using methods 4 with the linear background are shown in Fig. 13. The track match efficiency is found to be $(79.68 \pm 0.46)\%$.

The systematic error is determined by subtracting the method that gives the lowest efficiency by the method that gives the highest efficiency and then dividing by two. We obtain a track-match efficiency (ϵ^{CC}_{trk}) of $(79.68 \pm 0.51)\%$.

To determine the track match efficiency as a function of invariant mass, we model the track match efficiency using Monte Carlo, then normalize the distribution to data in the Z-peak region. We look at the efficiency for events to pass the requirement of at least one track match separately for forward and backward events and find that they are consistent. This is shown in Fig. 14. Therefore, we use the overall track match efficiency for all events. Figure 15 shows the Event track match efficiency versus invariant mass, which has been normalized to data. The decrease in efficiency below and above the Z-pole is due to a combination of bin migration and photon radiation.

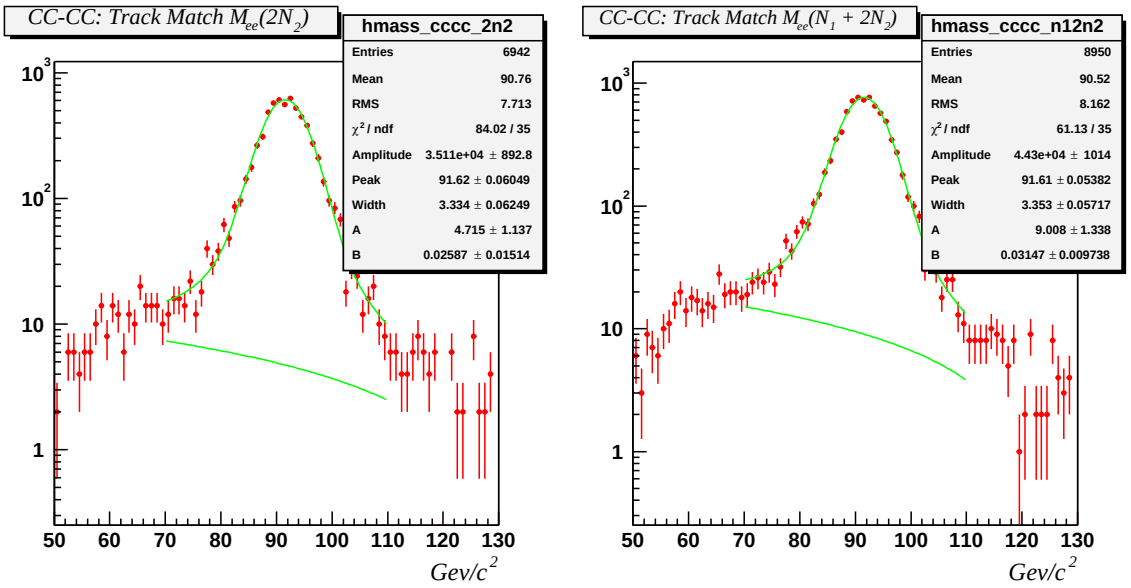

FIG. 13: Invariant mass distributions for the numerator (left) and denominator (right) in Eq. (10) used to calculate the track match efficiency with background subtraction methods 3 and 4. The points are the data and the lines show the linear background estimate and the result of the fit to a Breit-Wigner convolved with a Gaussian plus a linear background.

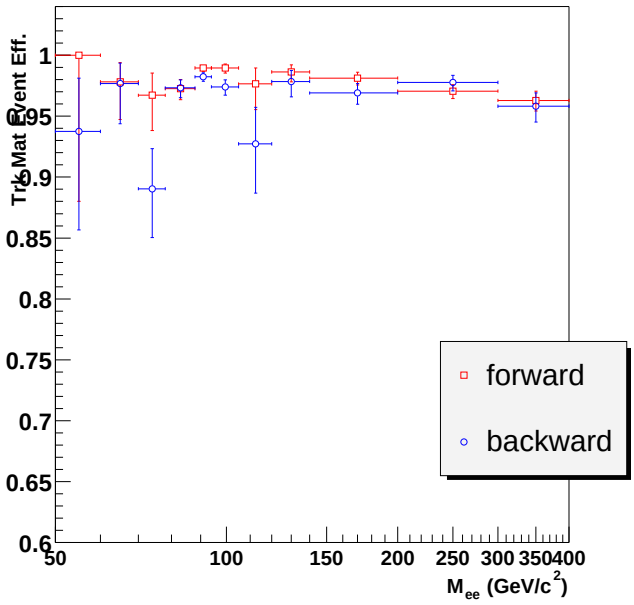

FIG. 14: Efficiency for Monte Carlo events to pass the requirement of at least one track match vs. M_{ee} for forward and backward events. The efficiencies are not normalized to data.

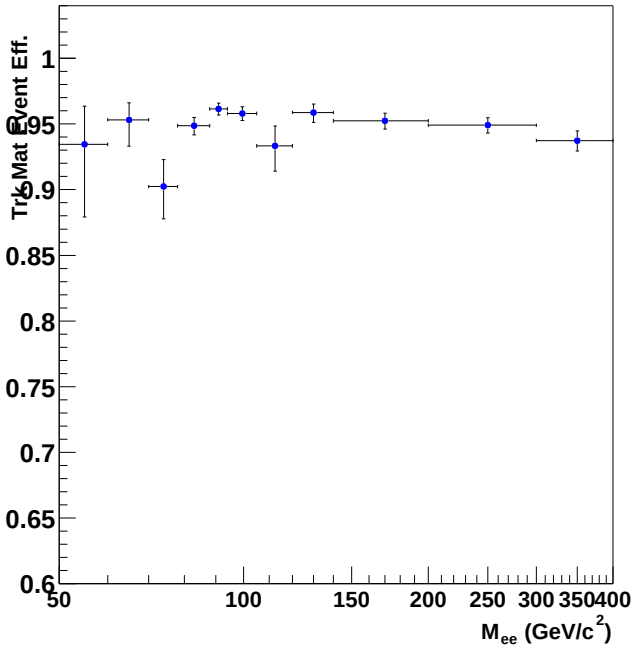

FIG. 15: Event track match efficiency vs. M_{ee} for all events. The efficiencies are normalized to data.

VII. BACKGROUNDS

The largest source of background for Drell-Yan events is the production of multijet and direct photon events, in which the jets have a large electromagnetic component (most of the energy is deposited in the EM section of the calorimeter) or they are mismeasured in some way that causes them to pass the electron selection criteria. This will be referred to as the QCD background. Other backgrounds are much smaller and originate mainly from $Z \rightarrow \tau\tau$, W + jets production, $t\bar{t}$ production ($t\bar{t} \rightarrow ee$), and diboson production ($W\gamma \rightarrow e\nu\gamma, WW \rightarrow ee, WZ \rightarrow ee, ZZ \rightarrow ee$).

To estimate the overall normalization of the QCD background, the matrix method is used. A relatively loose sample of M $\gamma^*/Z \rightarrow ee$ events are chosen by requiring events to contain two loose electrons (the *mother* sample). We then impose tighter cuts (requiring one of the electron candidates to have a track match), and obtain a *child* subsample containing P events which pass the tight cuts, and a subsample with F events that fail the tight cuts.

The mother sample actually contains three true subsamples: one with N_s signal events comprised of the real $\gamma^*/Z \rightarrow ee$ (but also including a small number of $\tau\tau$, $t\bar{t}$, and diboson events), one with B QCD background events, and one with B_W background events from the $W(\rightarrow e\nu) + X$ background. If the efficiencies for these subsamples to pass the tight cuts (relative to the loose cuts of the parent sample) are ϵ_s for the signal, ϵ_b for the QCD background events, and ϵ_w for the $W \rightarrow e\nu + X$ events, then the number of events passing and failing are

$$P = \epsilon_s N_s + \epsilon_b B + \epsilon_w B_W \tag{11}$$

$$F = (1-\epsilon_s) N_s + (1-\epsilon_b) B + (1-\epsilon_w) B_W \tag{12}$$

From the conservation of the total number of events in the parent sample:

$$M = P + F \tag{13}$$

The total number of QCD background events which pass the tight cuts is

$$N_{QCD} = \epsilon_b B \tag{14}$$

and the QCD background fraction is

$$f_{QCD} = \frac{N_{QCD}}{P}. \tag{15}$$

Solving for N_{QCD} we find

$$N_{QCD} = \epsilon_b \left(\frac{\epsilon_s M - P + (\epsilon_w - \epsilon_s) N_W}{\epsilon_s - \epsilon_b} \right) \tag{16}$$

Thus, the QCD background estimate can be obtained from the efficiencies and the estimate of the $W(\rightarrow e\nu) + X$ background (see Section VII D).

The signal efficiency for events requiring one tight and one loose electron, both in the CC, is related to the track match efficiency by:

$$\epsilon_s = \epsilon_{tm,CC}(2 - \epsilon_{tm,CC}) \tag{17}$$

where $\epsilon_{tm,CC}$ is the track match efficiency in the CC region described in Section VI. For the $W(\rightarrow e\nu) + X$ background we have

$$\epsilon_w = \epsilon_{tm,CC} \tag{18}$$

The QCD background efficiency is related to the fake track match probability by

$$\epsilon_b = \epsilon_{fake,CC}(2 - \epsilon_{fake,CC}) \tag{19}$$

where $\epsilon_{fake,CC}$ is the fake track match probability in the CC region.

A. Fake Track Match Probability

The fake track match probability is the probability that a QCD produced EM object having a fake track match. The same data sample as used for electron selection is used to determine the fake track match probability. Events must pass the luminosity quality and trigger requirements as used for the electron selection. Events with one jet candidate and one EM object are selected, and the requirement $\not\!\!E_T < 10$ GeV is imposed to remove W + jet events. The EM object must pass the "loose" electron criteria described above. Jet candidates are identified using the cone algorithm with $R = 0.7$.

The jet is required to pass the following good-jet criteria determined by the Jet-ID group:

- N90 > 1
- F90 < 0.65
- $0.05 <$ EM fraction < 0.7
- CHF < 0.25
- Hot fraction < 5.0
- $N_{trk} \geq 5$

where

N90 is the number of towers in a jet that contain 90% of the jet energy

F90 = N90/(total # of towers in a jet)

CHF is the course hadronic fraction of energy of the calorimeter clusters in jet section

Hot fraction cuts on cells of the calorimeter that have energy deposition not related to a real event

N_{trk} = number of tracks in a jet ($\Delta R < 0.5$). This cut reduces possible background from $Z \rightarrow \tau\tau$ decays

Figure 16 shows the N_{trk} distribution after all of the other jet cuts have been made. The p14 jet id is applied in d0correct by default, so we are starting with p14 jets with L1 confirmation. The p14 jet id gets rid of almost all "noise" jets, but we still apply the additional tighter cuts to make sure that no electrons remain in the jet sample. The electron candidate must be back-to-back with the good jet ($\Delta\phi(e - jet) > 2.5$). We then look to see if the electron candidate has a track matched to it. The probability that a QCD-produced EM object having a fake track match ("fake rate") is the fraction of these electron candidates which have a track match. The fake rate as a function of electron E_T is shown in Fig. 17. An overall systematic uncertainty of ±13% relative is assigned to the fake rate, because of variations of the fake rate as a function of pseudorapidity and transverse energy [14]. We assume that the fake rate does not vary with electron p_T and find the fake rate to be (1.6 ± 0.2)%.

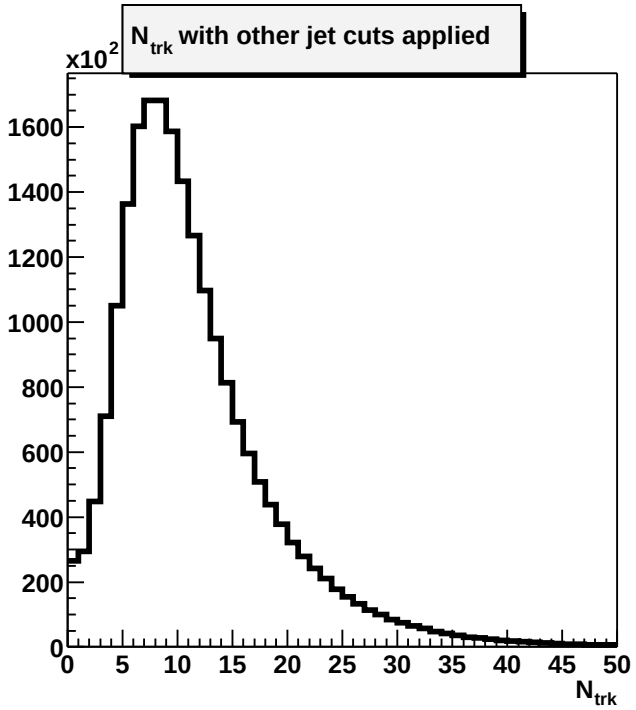

FIG. 16: N_{trk} distribution.

B. QCD Background Calculation

The shape of the background invariant mass distribution is obtained from di-EM events passing all the cuts used for the signal selection, except that the EM objects must fail the H-matrix chi-square cut: HMx8 > 35, and have no tracking requirement. These are predominantly dijet events. These events are also broken into forward and backward events to show that both are consistent within errors; therefore we use one shape for all events. This is shown in Fig. 18. The background is normalized using the matrix method described above. The mother sample (M) is selected by requiring two loose electrons and the Drell-Yan candidate event sample (P) is selected by requiring one tight electron and one loose electron. The resulting background distributions are shown in Fig. 19 and Fig. 20. The result for the estimated number of background events for 50 GeV $< M_{ee} <$ 400 GeV is $N_{QCD} = 102.2 \pm 13.1$

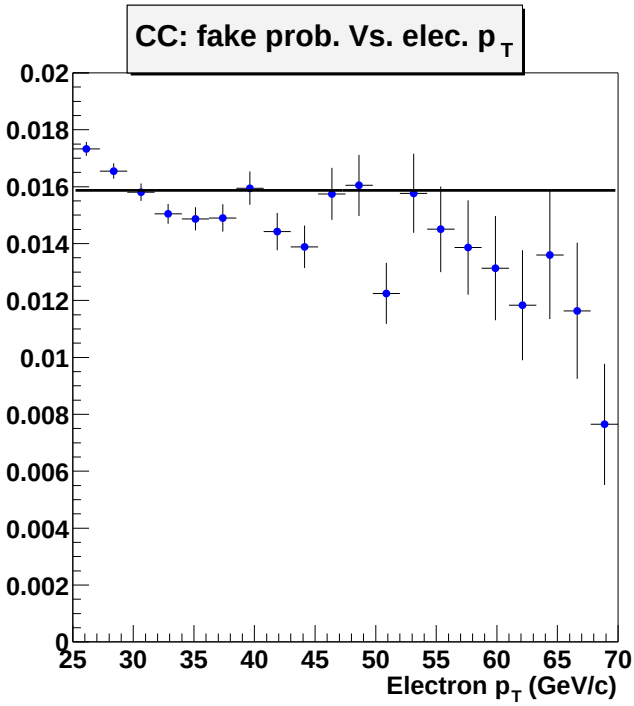

FIG. 17: Fake track match probability vs. electron E_T.

for all events, $N_{QCD} = 51.0 \pm 6.5$ for forward events, and $N_{QCD} = 51.2 \pm 6.6$ for backward events. The number of selected events in the data is $N_{data} = 5453 \pm 74$ for all events, $N_{data} = 2807 \pm 53$ for forward events, and $N_{data} = 2646 \pm 51$ for backward events. We find the QCD background fraction to be $f_{QCD} = 0.0188 \pm 0.0024$ for all events, $f_{QCD} = 0.0182 \pm 0.0023$ for forward events, and $f_{QCD} = 0.0194 \pm 0.0025$ for backward events.

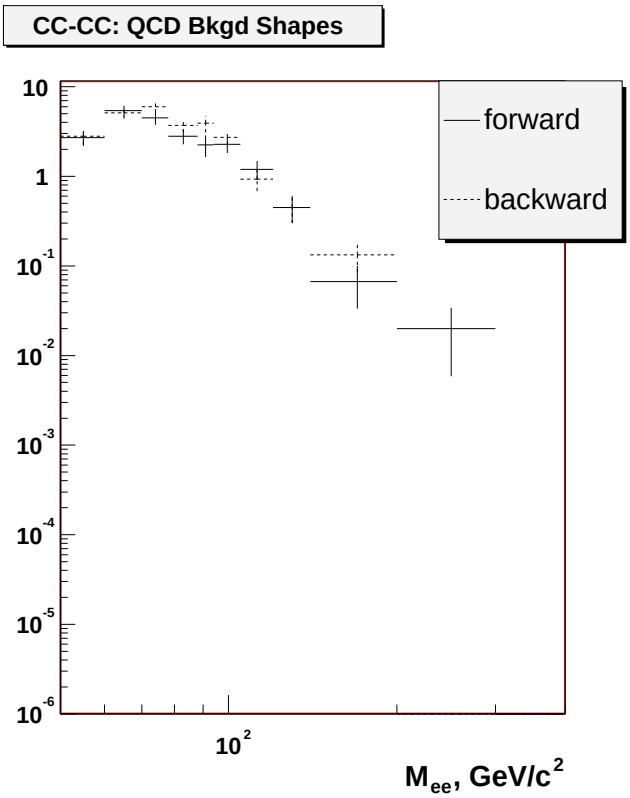

FIG. 18: QCD background shape for forward and backward events. Matrix method normalization has not been applied.

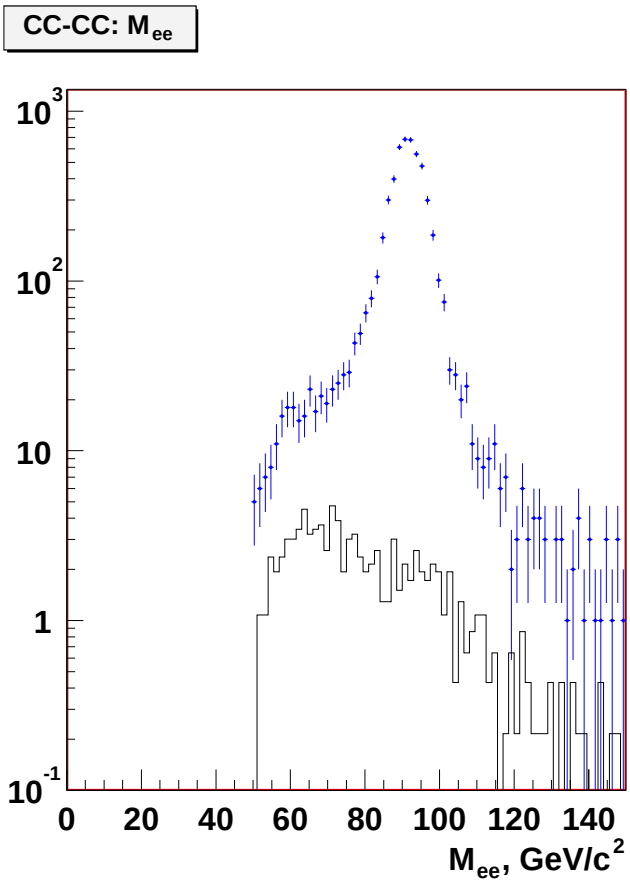

FIG. 19: Invariant mass distributions for data (solid circles with error bars) and estimated QCD background (histogram) in the mass region $50 < M_{ee} < 150$ GeV with 1.5 GeV bin width.

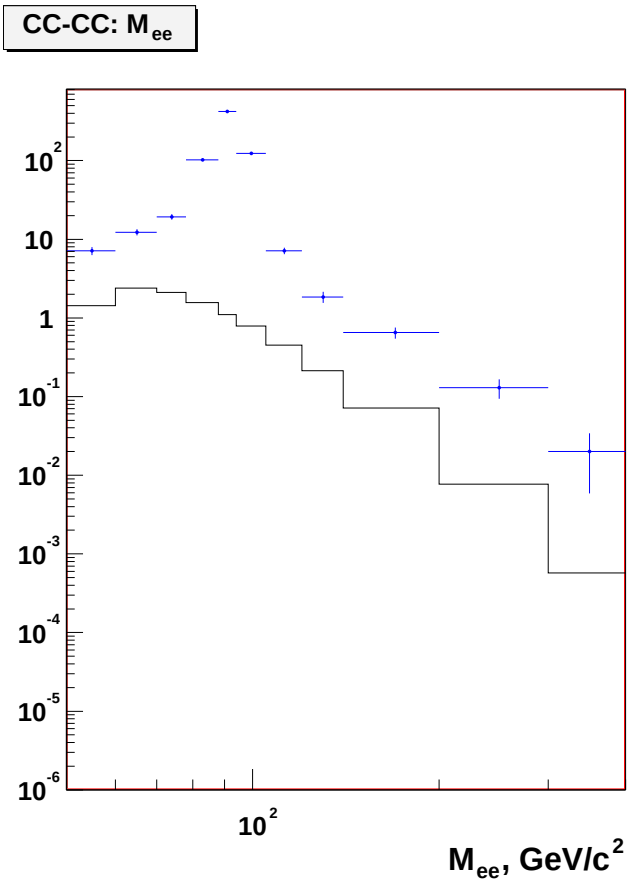

FIG. 20: Invariant mass distributions for data (solid circles with error bars) and estimated QCD background (histogram) in the mass region $50 < M_{ee} < 400$ GeV with variable bin width.

C. W + jets Background

The background from W + jets where a jet fakes an electron is obtained from a Monte Carlo sample of W + jets events and the probability for a jet to fake an electron. The fake probability is obtained from a jet data sample.

1. Probability for a Jet to Fake an Electron

Data from the Common Samples Group QCD skim is used to calculate the probability for a jet to fake an electron. The data sample is required to pass jet and minimum bias triggers. Events are required to pass one of the following two triggers:

- JT_25TT_NG: Two Level 1 calorimeter towers above 5 GeV, and a jet reconstructed at Level 3 with $E_T > 25$ GeV.
- JT_45TT: Two Level 1 calorimeter towers above 5 GeV, and a jet reconstructed at Level 3 with $E_T > 45$ GeV.

The lead jet (using the 0.5 cone algorithm) must pass the following jet quality requirements:

- $0.05 <$ Jet EM Fraction (EMF) < 0.90
- Jet Coarse Hadronic Fraction (CHF) < 0.4
- Jet Hot Fraction (HotF) < 10
- Jet N90 > 1
- Jet F90 < 0.5 or Jet CHF < 0.15,

and is required to pass the offline trigger requirements:

- Two Level 1 calorimeter towers above 5 GeV had to be matched to the lead jet. A match is defined as $\delta\phi_{det}(jet - tower) < 0.3$ and $\delta\eta_{det}(jet - tower) < 0.3$.
- The Level 3 jet must pass the appropriate Level 3 E_T threshold and be within $\Delta R(jet - tower) < 0.5$.

The lead jet must also pass the following tight jet cuts:

- $0.05 <$ Jet EMF < 0.7
- Jet CHF < 0.25
- Jet HotF < 5
- Jet N90 > 1
- $N_{trks} \geq 5$.
- $|\eta_{det}| < 1.1$.

The event must also have missing transverse energy $\not\!\!E_T < 10$ GeV.

After finding events with $\not\!\!E_T < 10$ GeV in which the lead jet passes the above requirements, we loop over the remaining jets (which are unbiased by the trigger requiremenbts) to find probe jets for the probability calculation. The probe jets must be separated from the lead jet by $\Delta R > 1.5$ and must pass the following jet quality cuts:

- $0.05 <$ Jet EMF < 0.95
- Jet CHF < 0.4
- Jet HotF < 10
- Jet N90 > 1
- $|\eta_{det}| < 1.1$.

We then find the number of EM objects passing the good electron requirements:

- id $= 10$ or $\pm$ 11
- EM Isolation < 0.15
- EMF > 0.9
- HMx7 $< 12 + slope \times (E_T - 45)$
- `in_fiducial`
- $p_T > 25$
- $|\eta_{det}| < 1.1$.

The EM objects were also required to be separated from the lead jet by $\Delta R > 1.5$ and separated from the probe jets by $\Delta R > 0.7$. The electron p_T was required to be less than the lead jet p_T. The fake probability is then equal to the number of good EM objects didvided by the total number of jets and EM objects passing the probe jet cuts:
We find the probability for a jet to fake an electron to be $P_{jet\to e} = 0.003$.

2. Calculation of the W + jets Background

To obtain invariant mass distribution of the W + jets background a Monte Carlo sample of $W(\to e\nu)$ + jets is used. The EM candidate is required to pass the same EM-id and track match requirements as used in the data signal selection and the jet candidates must pass the probe jet cuts used in the fake probability study above. The Monte Carlo events are then weighted by $P_{jet\to e}$ and efficiencies are applied using the efficiencies normalized to the data efficiencies. The invariant mass distribution of the resulting W + jets background is shown in Fig. 21.

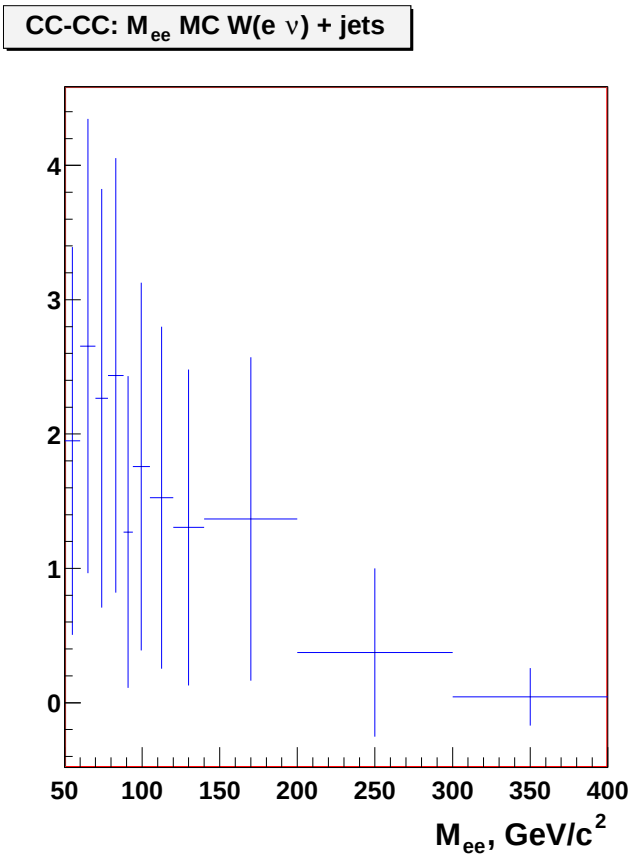

FIG. 21: Invariant mass distribution of background events from W + jets.

D. Other Backgrounds

Other backgrounds are much smaller and originate mainly from $Z \to \tau\tau$, $t\bar{t}$ production, and diboson production. These backgrounds are estimated from samples of Monte Carlo events that must pass acceptance cuts and are scaled by the event efficiencies derived from data and a K-factor of $\approx 1.2 - 1.4$, obtained from the ratio of the NLO cross section to the Monte Carlo generated cross section. We have considered the the following sources of additional backgrounds:

- $\gamma^*/Z \to \tau\tau$
- $t\bar{t} \to ee$
- $W\gamma \to e\nu\gamma$
- $WW \to ee$

Figure 22 shows the invariant mass distributions of these backgrounds. The total number of events from these backgrounds for each mass bin are given in Table III. All of these backgrounds, including the QCD and W + jets backgrounds, have been subtracted in the cross section calculation.

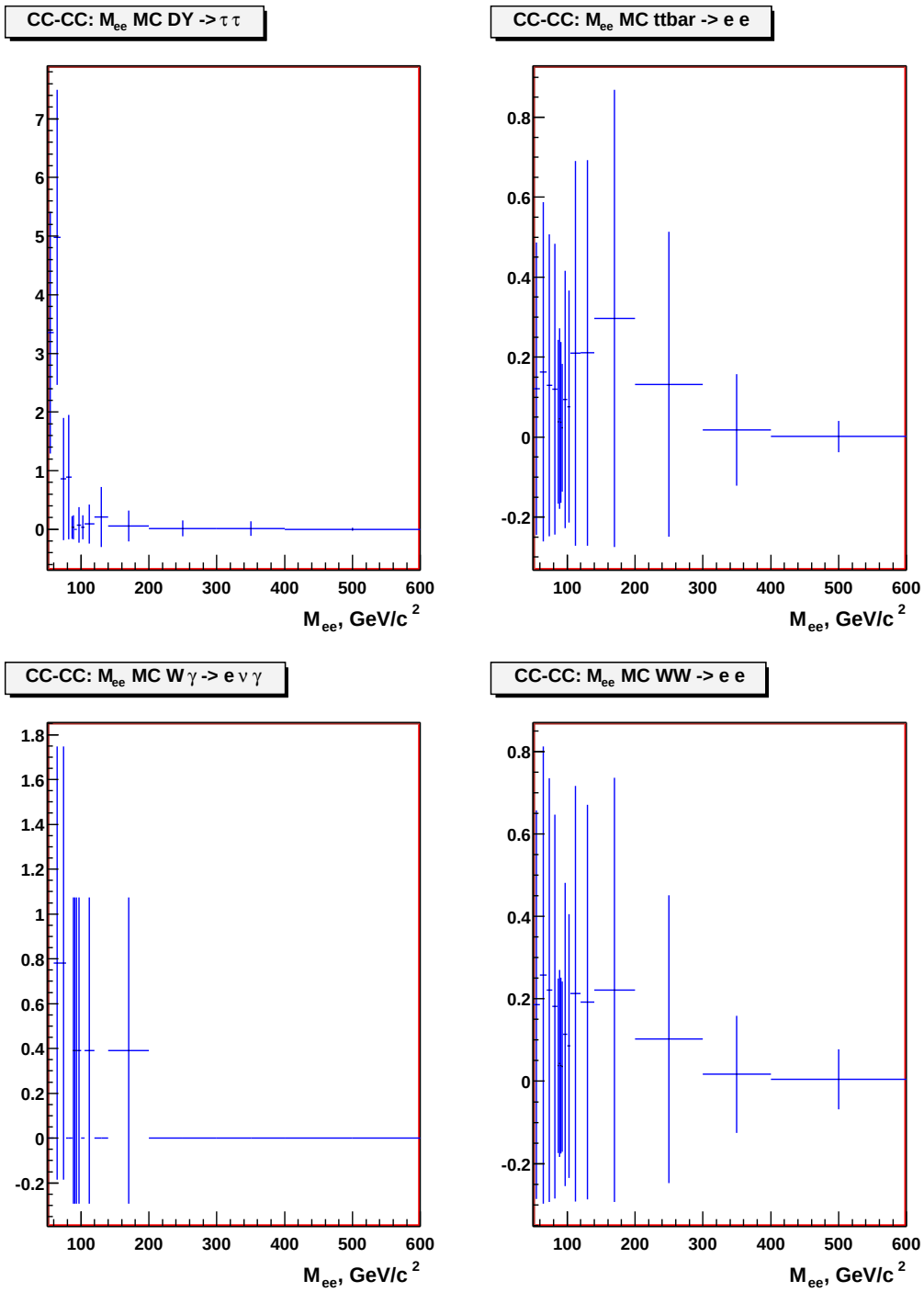

FIG. 22: Invariant mass distributions of background events from $\tau^+\tau^-$, $t\bar{t}$, $W\gamma$, and WW.

Mass Bin (GeV/c^2)	$\gamma^*/Z \to \tau\tau$	$t\bar{t} \to ee$	$W\gamma \to e\nu\gamma$	$WW \to ee$	$W(\to e\nu) + jets$
50 − 60	3.3790 ± 2.0770	0.1396 ± 0.3936	0.0000 ± 0.0000	0.1988 ± 0.4888	1.9488 ± 1.4425
60 − 70	4.1502 ± 2.3019	0.1574 ± 0.4179	0.3410 ± 0.5976	0.2701 ± 0.5698	2.6545 ± 1.6905
70 − 78	0.8595 ± 1.0473	0.1328 ± 0.3838	1.0231 ± 1.0394	0.2347 ± 0.5311	2.2661 ± 1.5584
78 − 88	0.8664 ± 1.0515	0.1656 ± 0.4287	0.3410 ± 0.5976	0.2347 ± 0.5311	2.4366 ± 1.6176
88 − 94	0.1257 ± 0.4005	0.1136 ± 0.3550	1.0231 ± 1.0394	0.1370 ± 0.4058	1.2708 ± 1.1601
94 − 105	0.0753 ± 0.3100	0.1779 ± 0.4443	0.3410 ± 0.5976	0.2108 ± 0.5033	1.7586 ± 1.3687
105 − 120	0.1473 ± 0.4335	0.2135 ± 0.4867	0.3410 ± 0.5976	0.2327 ± 0.5289	1.5259 ± 1.2732
120 − 140	0.2404 ± 0.5538	0.2190 ± 0.4929	0.0000 ± 0.0000	0.1978 ± 0.4876	1.3053 ± 1.1760
140 − 200	0.0944 ± 0.3471	0.3271 ± 0.6024	0.3410 ± 0.5976	0.2382 ± 0.5351	1.3682 ± 1.2045
200 − 300	0.0173 ± 0.1486	0.1382 ± 0.3916	0.0000 ± 0.0000	0.1121 ± 0.3671	0.3742 ± 0.6261
300 − 400	0.0096 ± 0.1105	0.0164 ± 0.1350	0.0000 ± 0.0000	0.0169 ± 0.1427	0.0440 ± 0.2142
50 − 400	9.9651 ± 3.5667	1.8011 ± 1.4137	3.9073 ± 3.7514	2.0837 ± 1.5826	16.953 ± 4.25392

TABLE III: Numbers of background events from $\tau^+\tau^-$, $t\bar{t}$, $W\gamma$, and WW for each mass bin. The last row gives the total backgrounds for the whole range 50-400 GeV.

VIII. COMPARISON OF MONTE CARLO AND DATA

The MC events are weighted by the factor (data integrated luminosity × cross section)/(total no. of events in mass range) to model equivalent data distributions. Since PYTHIA/PHOTOS Monte Carlo gives a lowest order (LO) cross section, a K-factor must be applied to include higher-order QCD corrections. For the comparison of the dielectron invariant mass distributions we use a mass-dependent K-factor. Since the MC was generated using the next-to-leading order (NLO) CTEQ6M PDF, we define the K-factor as

$$\text{K-factor} = \frac{\sigma(\alpha_s^2) \text{ with CTEQ6M}}{\sigma(\alpha_s^0) \text{ with CTEQ6M}}. \tag{20}$$

The cross sections are obtained from the calculation of van Neerven [13]. The van Neerven code allows evaluation of the leading order cross section, as well as the cross section to order α_s^2. The K-factor for each bin is calculated at the invariant mass equal to the average M_{ee} in the bin as calculated using the Monte Carlo. The K-factor as a function of $\overline{M_{ee}}$ is shown in Fig. 23. To compare the Monte Carlo to the data, Monte Carlo events must pass the acceptance cuts, and are then weighted by the M_{ee}-dependent K-factor and the total efficiency obtained from data. Figures 24 and 25 show a comparison of the invariant mass distributions of Monte Carlo and data. Figure 26 shows the fractional difference between Monte Carlo and data as a function of M_{ee}: $(N_{data} - N_{theory})/N_{theory}$, where N is the number of events in each mass bin. Other data distributions are compared with Monte Carlo by applying the acceptance cuts, and then normalizing the MC to the data.

The electron E_T distribution is shown in Fig. 27. Figure 28 shows the detector η distribution. The electron ϕ distribution is shown in Fig. 29. Figure 30 shows the cos θ^* distribution, where θ^* is the polar angle of the electron in the Collins-Soper frame.

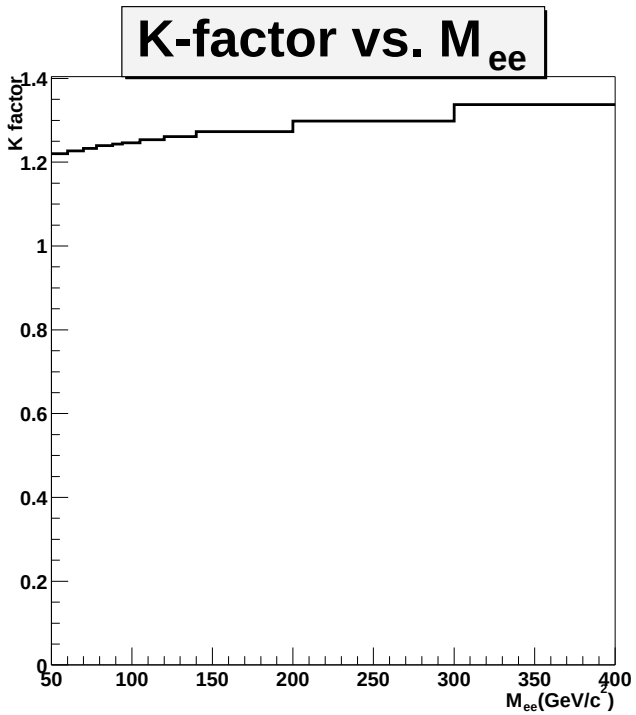

FIG. 23: K-factor as a function of invariant mass.

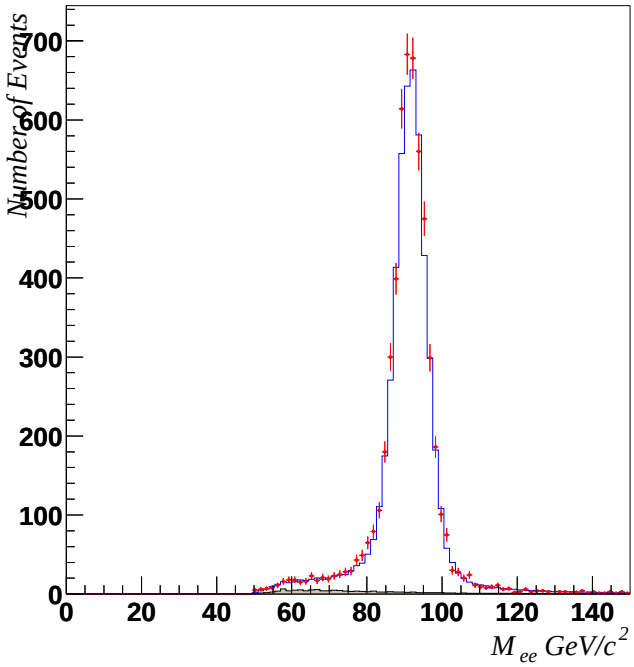

FIG. 24: Comparison of the invariant mass distribution from data with that from Monte Carlo for $M_{ee} < 150$ GeV/c^2. The red points are data with statistical errors only. The blue line is the sum of the Drell-Yan Monte Carlo and the total background estimate. The green dashed line is the sum of the estimated backgrounds, and the brown shaded histogram is the QCD background only.

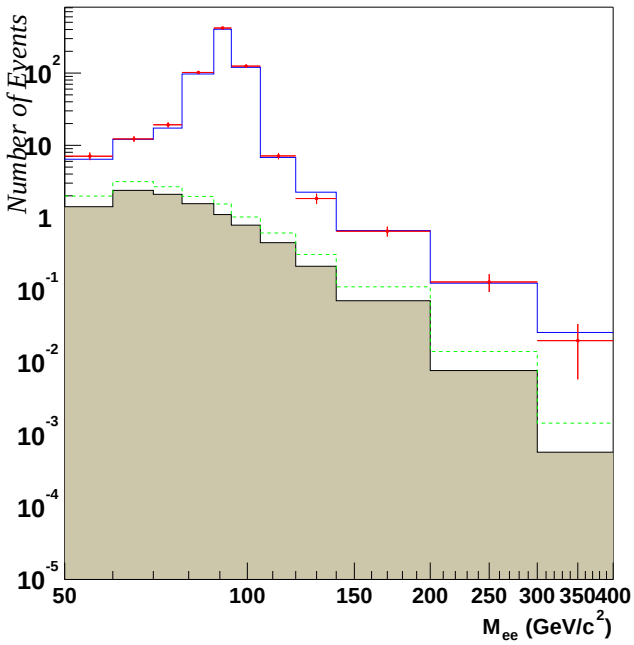

FIG. 25: Comparison of the invariant mass distribution from data with that from Monte Carlo for $50 < M_{ee} < 400$ GeV/c^2. The red points are data with statistical errors only. The blue line is the sum of the Drell-Yan Monte Carlo and the total background estimate. The green dashed line is the sum of the estimated backgrounds, and the brown shaded histogram is the QCD background only.

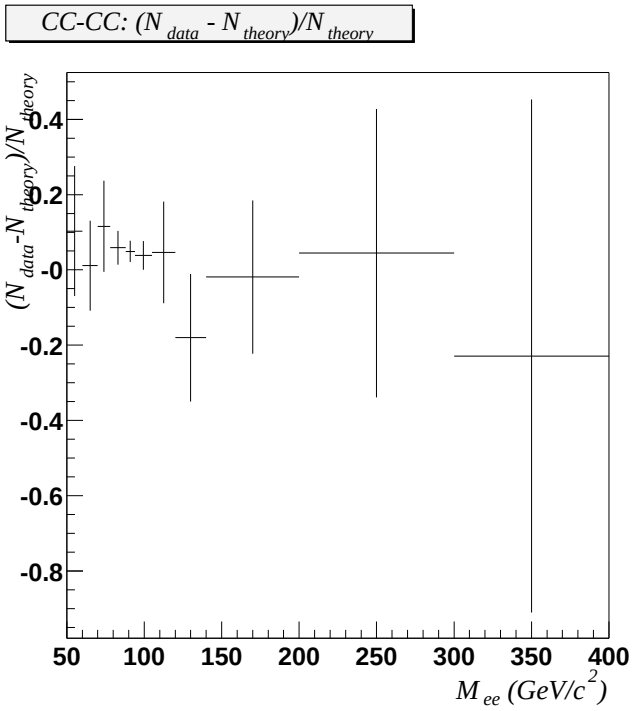

FIG. 26: Comparison of PYTHIA/PHOTOS predictions with the data.

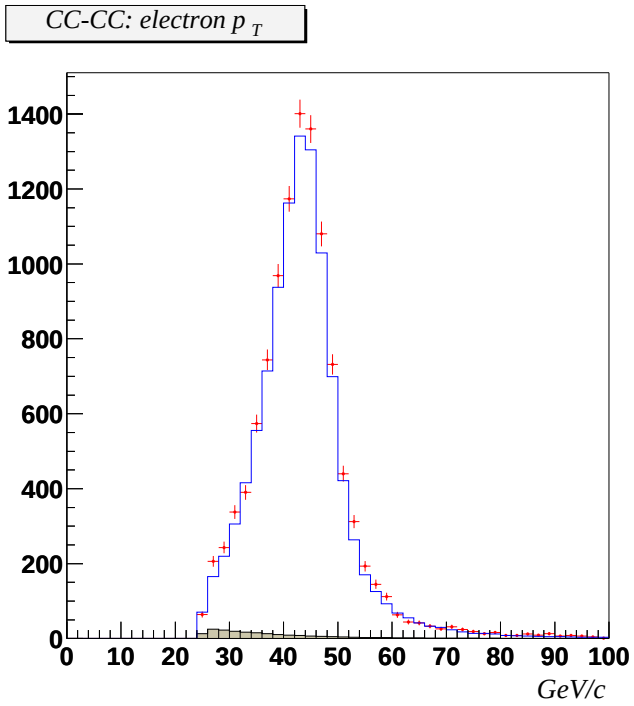

FIG. 27: Comparison of the electron transverse momentum distribution from data with that from Monte Carlo. The red points are data with statistical errors only, the blue line is the sum of the Drell-Yan Monte Carlo and the background estimate, and the brown shaded histogram is the QCD background.

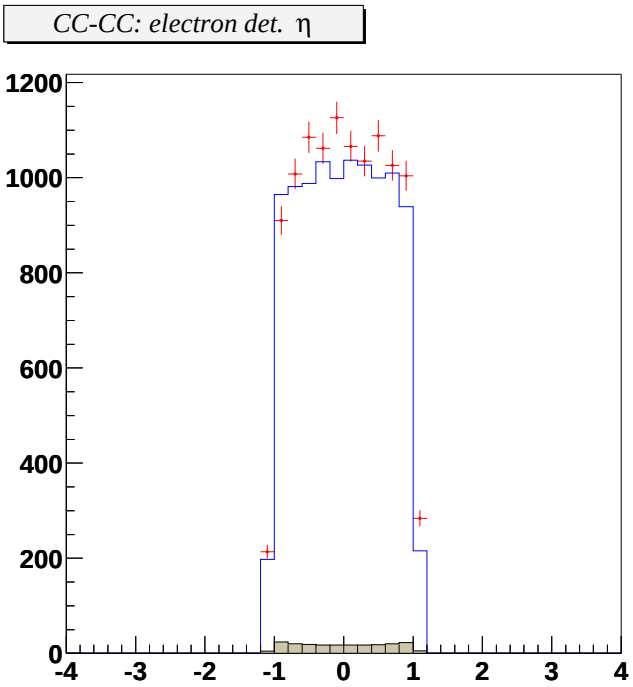

FIG. 28: Comparison of the electron detector eta distribution from data with that from Monte Carlo. The red points are data with statistical errors only, the blue line is the sum of the Drell-Yan Monte Carlo and the background estimate, and the brown shaded histogram is the QCD background.

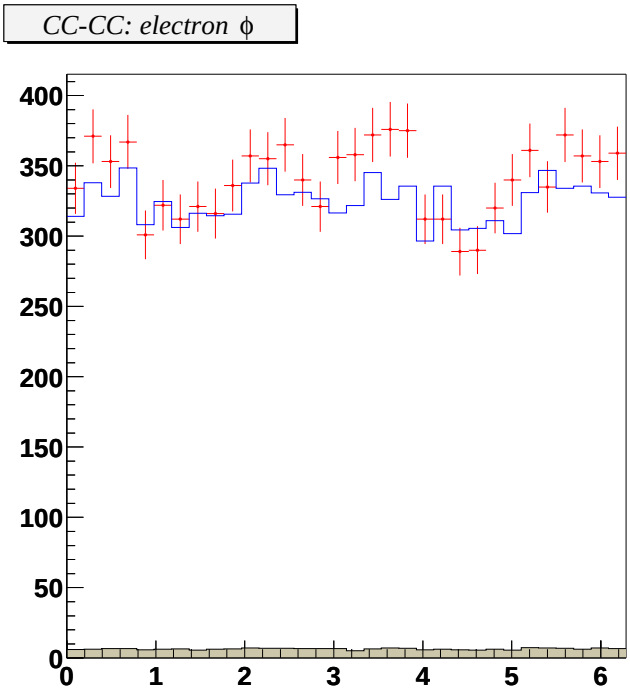

FIG. 29: Comparison of the electron phi distribution from data with that from Monte Carlo. The red points are data with statistical errors only, the blue line is the sum of the Drell-Yan Monte Carlo and the background estimate, and the brown shaded histogram is the QCD background.

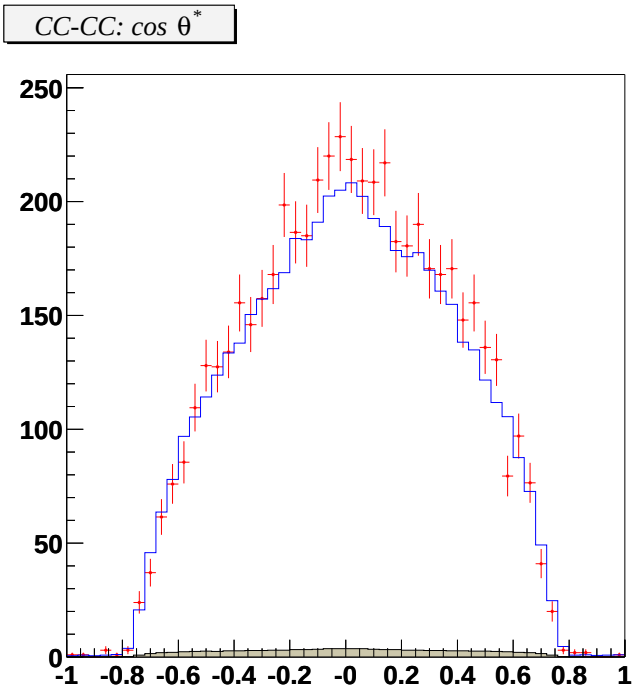

FIG. 30: Comparison of the cos θ^* distribution from data with that from Monte Carlo. The red points are data with statistical errors only, the blue line is the sum of the Drell-Yan Monte Carlo and the background estimate, and the brown shaded histogram is the QCD background.

A. Uncorrected Forward-Backward Asymmentry

In this section we compare the measured forward-backward asymmetry with predictions of the Monte Carlo simulation. The measured or "raw" asymmetry is defined by

$$A_{FB}^{raw} = \frac{(N_F - B_F) - (N_B - B_B)}{(N_F - B_F) + (N_B - B_B)} \tag{21}$$

where N_F, N_B are the observed number of forward and backward events in the data, and B_F, B_B are the estimated backgrounds for forward and backward events, respectively. The data are not corrected for kinematic acceptance, geometric acceptance, detector resolution, or QED radiation effects.

First we show the observed and predicted cos θ^* distributions in each e^+e^- invarient mass bin; see Figures 31 and 32. The plots show the data compared with the expectation from the sum of the Monte Carlo signal and total background estimate. Good agreement is seen between data and the SM predictions for all eleven mass regions. Also shown are the generator-level cos θ^* distributions with no kinematic or geometric acceptance cuts applied.

The raw forward-backward asymmetry from data is shown in Fig. 33, and is compared to the Monte Carlo prediction. Good agreement between the data and the standard model prediction is seen; the chi-square per degree of freedom is $\chi^2/dof = 1.47$.

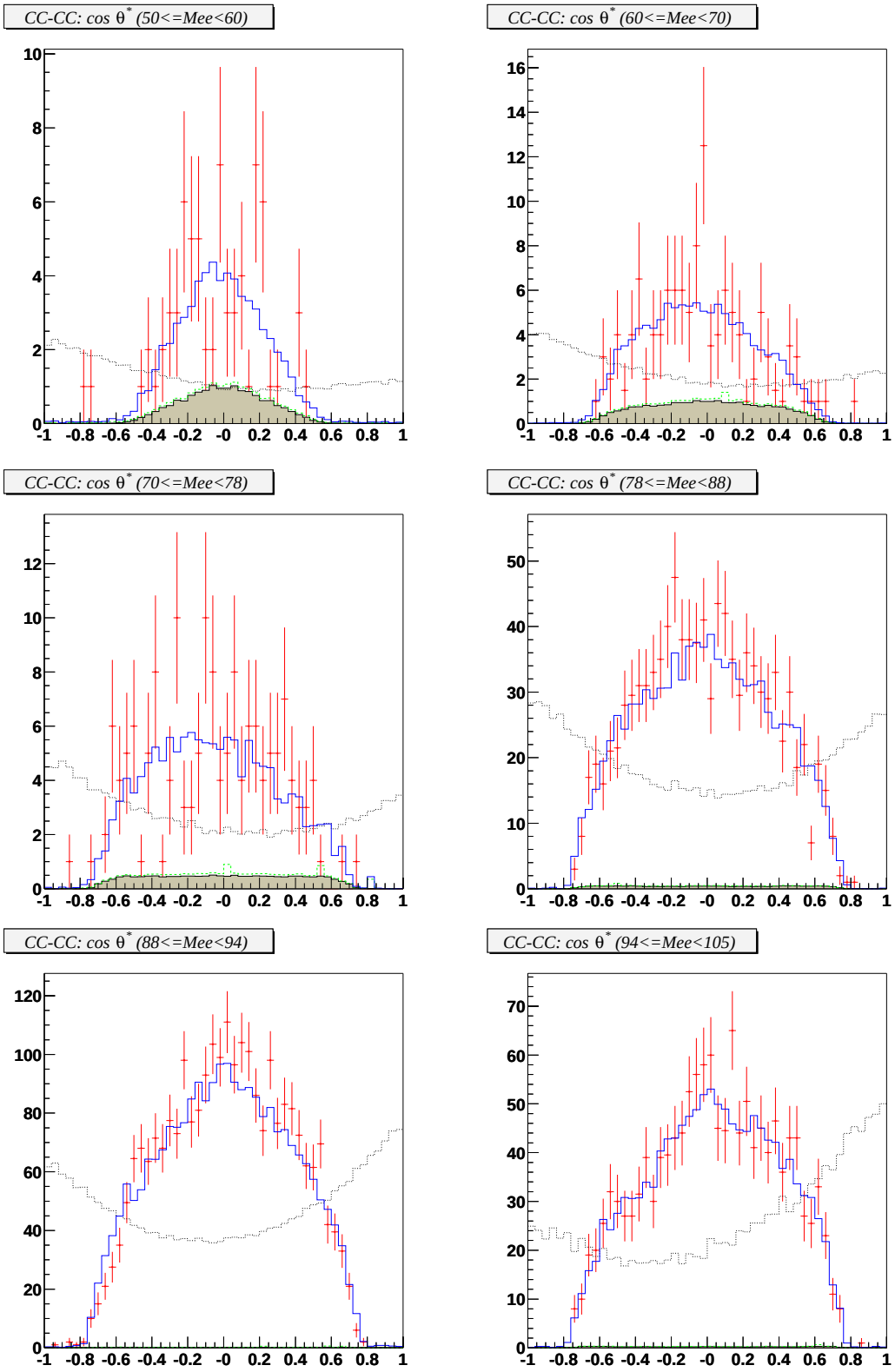

FIG. 31: Comparison of the cos θ^* distributions from data with those from Monte Carlo in M_{ee} bins from 50 GeV/c^2 to 105 GeV/c^2. The points are data with statistical errors only. The solid line is the sum of the Drell-Yan Monte Carlo and the background estimate, the shaded histogram is the QCD background only, and the dashed histogram is the total background. The dotted histogram shows the generator-level distribution for the signal before selection cuts are applied.

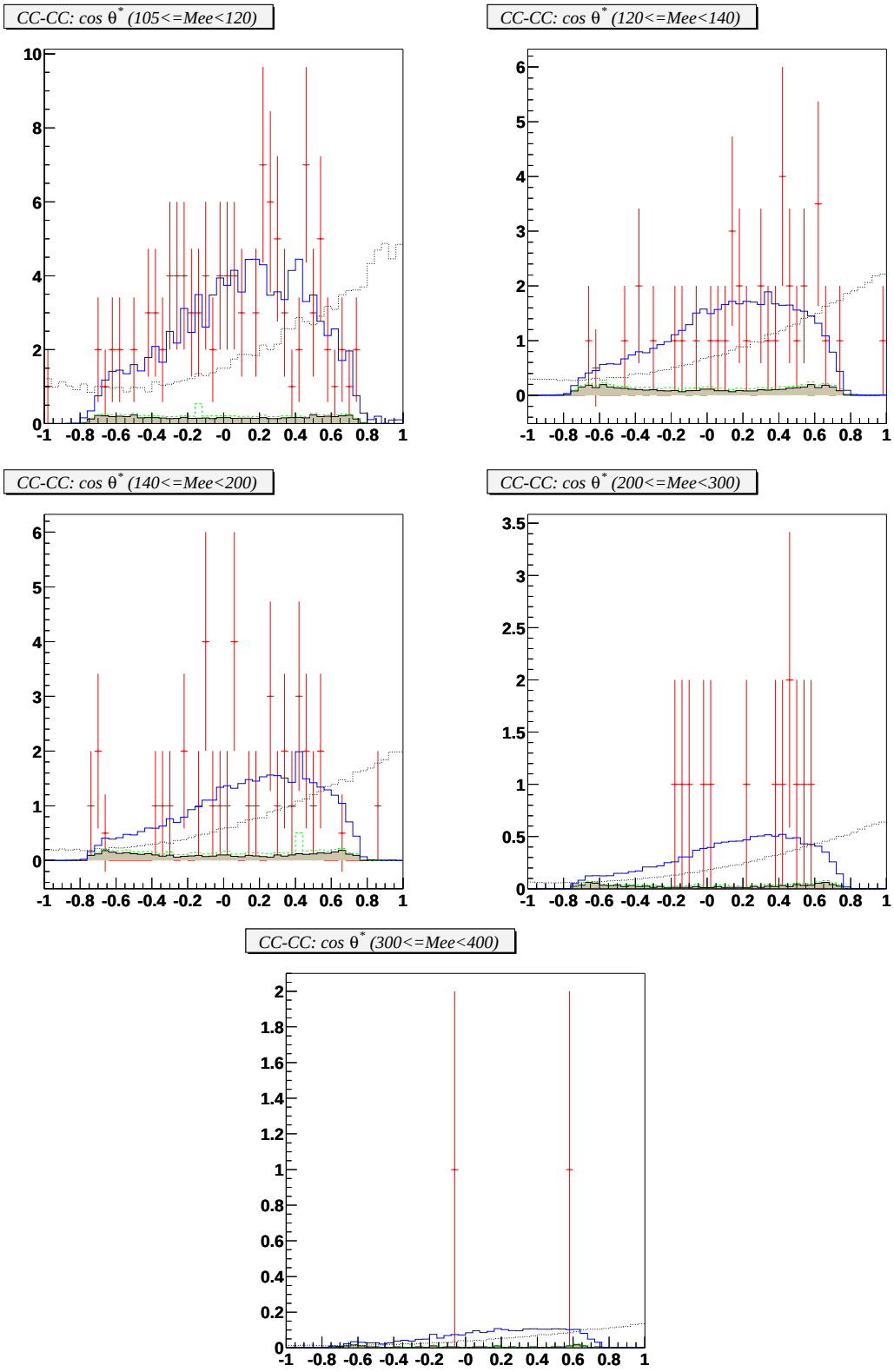

FIG. 32: Comparisons of the cos θ^* distribution from data with that from Monte Carlo in M_{ee} bins from 105 GeV/c^2 to 400 GeV/c^2. The points are data with statistical errors only. The solid line is the sum of the Drell-Yan Monte Carlo and the background estimate, the shaded histogram is the QCD background only, and the dashed histogram is the total background. The dotted histogram shows generator level distribution for the signal before selection cuts are applied.

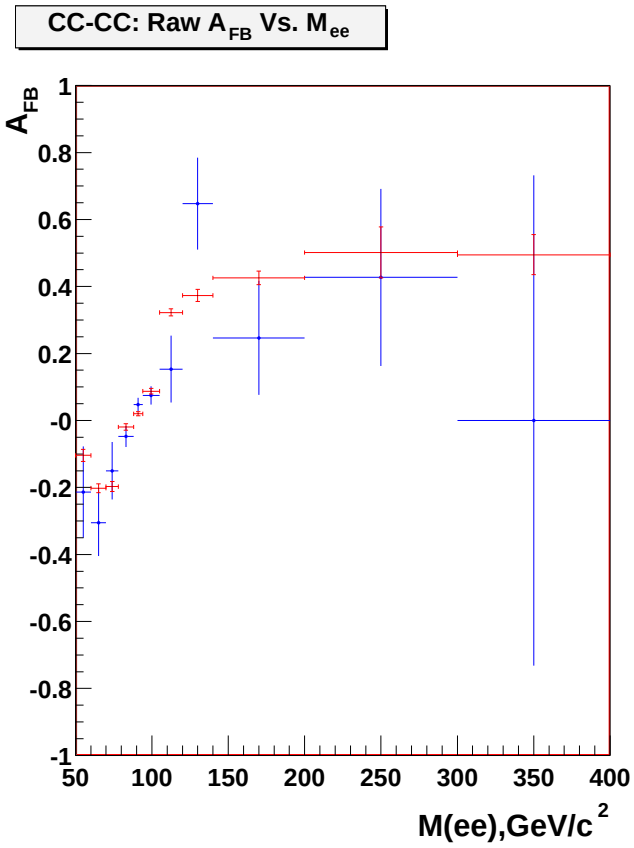

FIG. 33: Comparison of the raw forward-backward asymmetry distribution from data with the prediction of the Monte Carlo. The blue points are data with statistical errors only and the red line is the Drell-Yan Monte Carlo.

IX. UNFOLDING CORRECTION

This section describes the unfolding method used to correct for kinematic cuts, geometrical acceptance, effects of the detector resolution, and QED radiation effects.

A. QED Radiative Corrections

The effect of QED radiation on the measured Drell-Yan differential cross section and forward-backward asymmetry is corrected for in order to obtain a Born-level cross section. This allows easy comparison with Born-level predictions and with results from other experiments. Purely weak corrections are very small and can be ignored [15, 16]. The largest QED corrections come from final state photon bremsstrahlung; the initial state QED corrections are negligible. $\mathcal{O}(\alpha)$ QED corrections and $\mathcal{O}(\alpha_s)$ QCD corrections are small (and have opposite sign) above the $Z-$peak region. QED corrections are significantly larger in the lower mass regions 50 GeV $< M_{ee} <$ 100 GeV.

If detector effects are taken into account, the QED corrections are reduced, but are still sizable. This reduction occurs because the calorimeter has a finite resolution, and an electron and photon with a small opening angle will be measured as one EM object. The QED radiative corrections are taken into account in the unfolding correction. In this analysis, we correct for final state QED bremsstrahlung effects only.

B. Calculation of the Unfolding Correction

The Monte Carlo events described in Section II are used to obtain the unfolding correction. The unfolding correction β is calculated in bins of dielectron invariant mass and is used to correct for the kinematic cuts and geometrical acceptance, the effects of the detector resolution, and the QED correction factor. An estimate of the unfolded (i.e. true) invariant mass distribution is computed by multiplying each bin i of the observed experimental distribution by the ratio of the "true" to the "observed" Monte Carlo event numbers:

$$d_i^{true} = \frac{m_i}{m_i'} \cdot d_i^{obs} \equiv \frac{d_i^{obs}}{\beta_i} \tag{22}$$

where $\beta_i = m_i'/m_i$ is the ratio of the "observed" to the "true" Monte Carlo event numbers. We use this unfolding technique to obtain the true invariant mass distribution and (after dividing by the efficiency and integrated luminosity) the differential cross section.

Therefore, the unfolding correction in each bin is defined by

$$\beta_i = \frac{m_i'}{m_i} \tag{23}$$

where m_i' is the number of Drell-Yan Monte Carlo events passing kinematic and acceptance cuts with reconstructed mass M_{ee} in bin i, and m_i is the number of generated Drell-Yan Monte Carlo events without final state QED radiation with generator-level mass M_{ee} in bin i.

The Monte Carlo events used to obtain the unfolding correction are generated in five mass regions (see Table I). The events in each mass region are weighted to account for the

different cross section in each range. The unfolding correction is calculated in each mass bin using Eq. (23), and the error is given by

$$\delta\beta_i = \sqrt{\frac{1}{D^2}\delta N^2 + \frac{N^2}{D^4}\delta D^2} \tag{24}$$

where $N \equiv m' = \sum_{j=1}^{5} w_j n_j$ and $D \equiv m_\mu = \sum_{j=1}^{5} w_j^{'} n_j^{'}$, n_j is the number of events in bin i from Monte Carlo event sample j, and the sum runs over all five Monte Carlo event samples. The weights are given by $w_j = (\mathcal{L} * \sigma_j)/N_j$, where σ_j and N_j are the cross section and generated number of events in the j^{th} Monte Carlo event sample. The error on the number of events is $\delta n_j = \sqrt{n_j}$ and $\delta n_j^{'} = \sqrt{n_j^{'}}$.

The kinematic and acceptance cuts applied to the events in the numerator of Eq. (23) are:

- 2 EM objects with
  - ID = 10 or ± 11
  - in fiducial regions
  - in CC region
  - $E_T^{smeared} > 25$ GeV/c

The unfolding correction for forward and backward events is shown in Fig. 34, and for all events in Fig. 35, and is used to determine the unfolded Drell-Yan differential cross section. The dip at the Z-pole is due mostly to to detector resolution effects. At high invariant mass the unfolding correction is smaller for forward events than for backward events because the asymmetry is large and positive in this region ($A_FB \approx 0.6$). This means that more events are far forward and fall outside the acceptance of the central calorimeter.

For reference, we also calculate an unfolding correction using events with FSR and generator-level invariant mass in the numerator and denominator of Eq. (23). This unfolding correction does not account for detector resolution effects or QED radiation effects and is calculated for illustrative purposes only (it is not used in the analysis). This is shown for forward and backward events in Fig. 36, and for all events in Fig. 37.

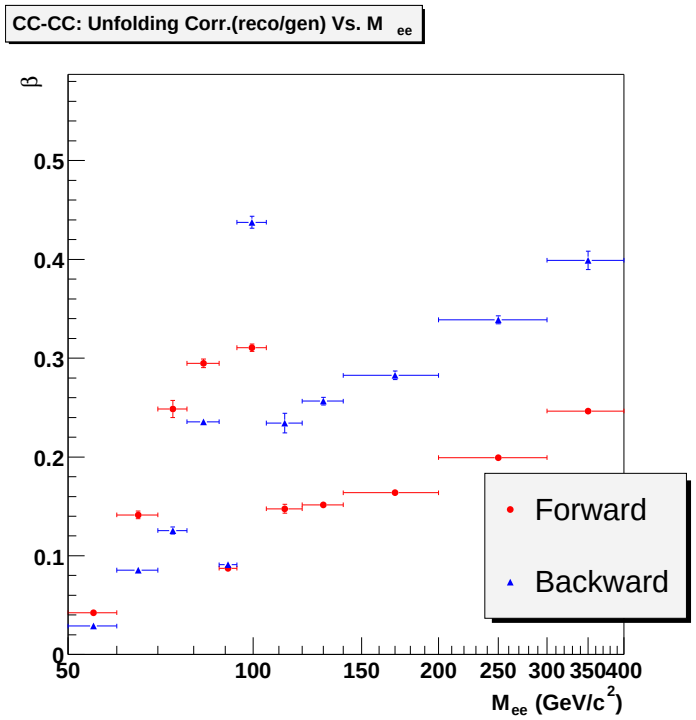

FIG. 34: Unfolding correction β for forward and backward events.

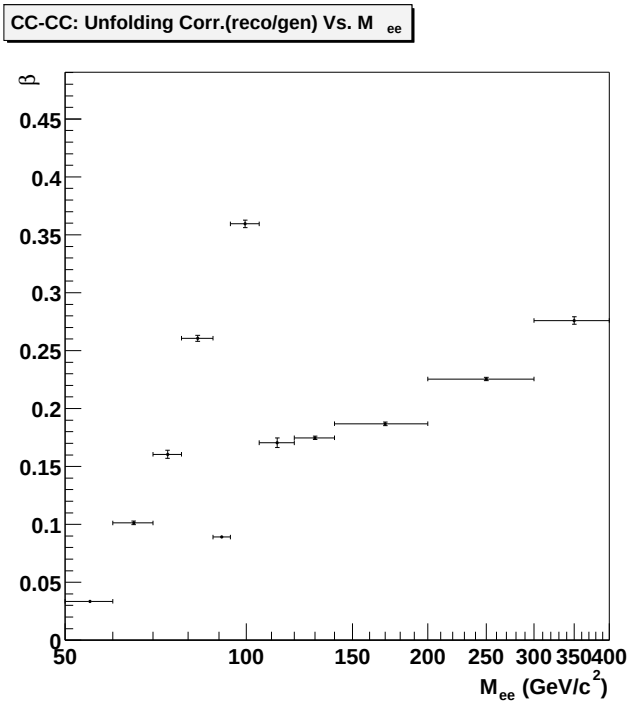

FIG. 35: Unfolding correction β for all events (i.e. the sum of the forward and backward events).

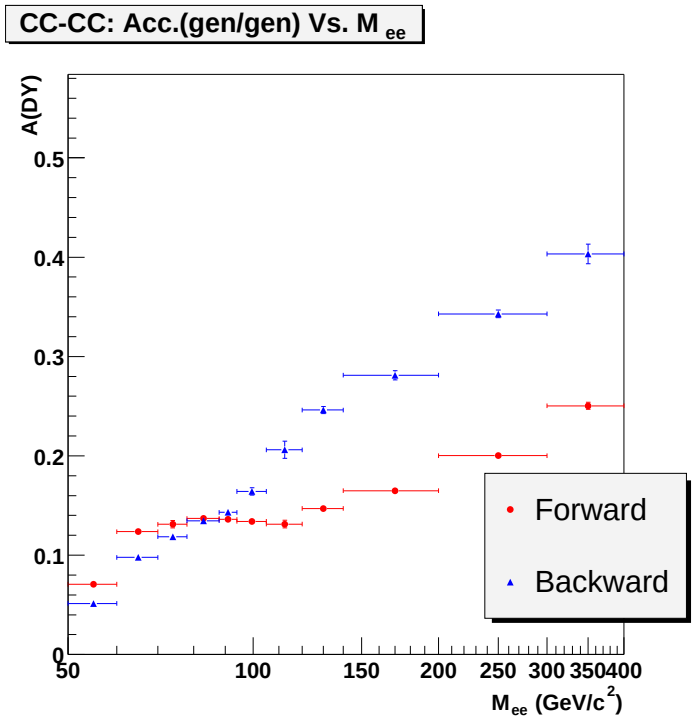

FIG. 36: Unfolding correction calculated with no detector resolution effects and no QED correction effects for forward and backward events.

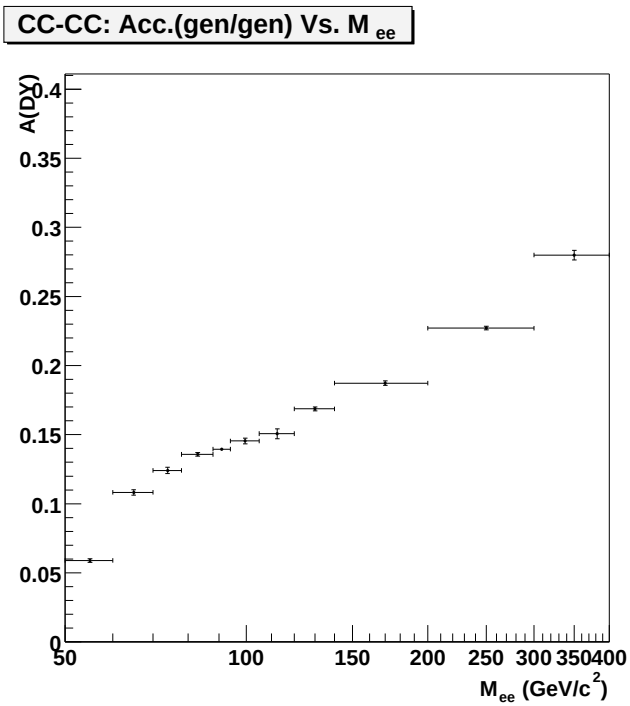

FIG. 37: Unfolding correction calculated with no detector resolution effects and no QED correction effects for all events.

The systematic error for each of the PMCS parameters is determined by varying one parameter from its central value by $\pm 1\sigma$, while leaving the other parameters at fixed, then re-calculating the unfolding correction for each mass bin. The systematic error on the unfolding correction for each PMCS parameter would then be $(\beta_{+1\sigma} - \beta_0)$ and $(\beta_0 - \beta_{-1\sigma})$, where β_0 is the value of β when the central value of the PMCS parameter is used. Here we have used a conservative estimate by taking the larger error as a symmetric error. Table IV shows the systematic errors due to the PMCS scale parameter α for each M_{ee} bin for forward, backward, and all events, respectively. Tables V and VI show the systematic errors due to the PMCS energy offset δ and constant term C in each M_{ee} bin for forward, backward, and all events.

The systematic error for the PMCS electron-photon merging angle is determined by varying ΔR by ± 0.1, while leaving the other PMCS parameters fixed, then re-calculating the unfolding correction for each mass bin. The systematic error for each of the above parameters would then be $(\beta_{0.3} - \beta_{0.2})$ and $(\beta_{0.2} - \beta_{0.1})$, where $\beta_{0.2}$ is the value of β obtained with $\Delta R = 0.2$. Here we have used a conservative estimate by taking the larger error as a symmetric error. Table VII shows the systematic errors due to the PMCS ΔR parameter in M_{ee} bin for forward, backward, and all events, respectively.

The systematic error due to the PDF uncertainty is calculated using the CTEQ6 prescription [8]:

$$\delta X_{\pm} = \sum_{k=1}^{n} [X(a_i^{\pm}) - X(a_0)]^2, \tag{25}$$

where X is the observable (i.e. the unfolding correction factor β in our case), $X(a_i^{\pm})$ is the result for X based on the i^{th} PDF error set, and $X(a_0)$ is the result for X based on the central PDF set CTEQ6M. where one must sum up all the values of the observable displaced in the positive direction from the central value and all the values of the The unfolding correction factor is calculated for CTEQ6M and all 40 error PDFs for each mass bin using 40 Monte Carlo samples with and without QED FSR. Each smaple is comprised of 150,000 events. This gives an asymmetric PDF systematic error for each invariant mass bin. Table VIII shows the PDF systematic errors for forward, backward, and all events for each mass bin.

The systematic error due to uncertainty in transverse momentum of the e^+e^- system is determined by varying the generated $p_T(e^+e^-)$ distribution in the PYTHIA event generator. We take the largest difference between the unfolding correction calculated with the default Monte Carlo and the unfolding correction calculated with two alternatives: (a) a CDF p_T^Z-tuned PYTHIA Monte Carlo [9]; and (b) a DØ p_T^Z-tuned Monte Carlo [10]. Table IX shows the systematic errors due to the $p_T(e^+e^-)$ uncertainty for each M_{ee} bin for forward, backward, and all events.

Mass Region (GeV/c^2)	σ_F^{sys}	σ_B^{sys}	σ_{ALL}^{sys}
$50 < M_{ee} < 60$	± 0.0013	± 0.0009	± 0.0003
$60 < M_{ee} < 70$	± 0.0031	± 0.0013	± 0.0003
$70 < M_{ee} < 78$	± 0.0180	± 0.0055	± 0.0077
$78 < M_{ee} < 88$	± 0.0284	± 0.0180	± 0.0223
$88 < M_{ee} < 94$	± 0.0020	± 0.0012	± 0.0012
$94 < M_{ee} < 105$	± 0.0325	± 0.0352	± 0.0336
$105 < M_{ee} < 120$	± 0.0053	± 0.0044	± 0.0040
$120 < M_{ee} < 140$	± 0.0031	± 0.0073	± 0.0029
$140 < M_{ee} < 200$	± 0.0025	± 0.0062	± 0.0026
$200 < M_{ee} < 300$	± 0.0030	± 0.0037	± 0.0032
$300 < M_{ee} < 400$	± 0.0040	± 0.0087	± 0.0042

TABLE IV: Systematic error in unfolding correction β due to the uncertainty in the EM energy scale parameter. Errors are shown separately for forward, backward, and all events.

Mass Region (GeV/c^2)	σ_F^{sys}	σ_B^{sys}	σ_{ALL}^{sys}
$50 < M_{ee} < 60$	± 0.0012	± 0.0002	± 0.0003
$60 < M_{ee} < 70$	± 0.0077	± 0.0009	± 0.0019
$70 < M_{ee} < 78$	± 0.0162	± 0.0042	± 0.0016
$78 < M_{ee} < 88$	± 0.0114	± 0.0081	± 0.0053
$88 < M_{ee} < 94$	± 0.0021	± 0.0009	± 0.0009
$94 < M_{ee} < 105$	± 0.0140	± 0.0114	± 0.0130
$105 < M_{ee} < 120$	± 0.0034	± 0.0082	± 0.0036
$120 < M_{ee} < 140$	± 0.0004	± 0.0067	± 0.0015
$140 < M_{ee} < 200$	± 0.0015	± 0.0031	± 0.0015
$200 < M_{ee} < 300$	± 0.0013	± 0.0061	± 0.0022
$300 < M_{ee} < 400$	± 0.0038	± 0.0042	± 0.0039

TABLE V: Systematic error in unfolding correction β due to the uncertainty in the EM energy offset parameter. Errors are shown separately for forward, backward, and all events.

Mass Region (GeV/c^2)	σ_F^{sys}	σ_B^{sys}	σ_{ALL}^{sys}
$50 < M_{ee} < 60$	± 0.0009	± 0.0005	± 0.0003
$60 < M_{ee} < 70$	± 0.0114	± 0.0007	± 0.0037
$70 < M_{ee} < 78$	± 0.0238	± 0.0044	± 0.0036
$78 < M_{ee} < 88$	± 0.0207	± 0.0082	± 0.0076
$88 < M_{ee} < 94$	± 0.0035	± 0.0029	± 0.0025
$94 < M_{ee} < 105$	± 0.0063	± 0.0067	± 0.0044
$105 < M_{ee} < 120$	± 0.0032	± 0.0099	± 0.0028
$120 < M_{ee} < 140$	± 0.0014	± 0.0055	± 0.0023
$140 < M_{ee} < 200$	± 0.0008	± 0.0019	± 0.0010
$200 < M_{ee} < 300$	± 0.0012	± 0.0032	± 0.0012
$300 < M_{ee} < 400$	± 0.0020	± 0.0055	± 0.0017

TABLE VI: Systematic error in unfolding correction β due to the uncertainty in the EM energy resolution constant term. Errors are shown separately for forward, backward, and all events.

Mass Region (GeV/c^2)	σ_F^{sys}	σ_B^{sys}	σ_{ALL}^{sys}
$50 < M_{ee} < 60$	± 0.0022	± 0.0001	± 0.0007
$60 < M_{ee} < 70$	± 0.0072	± 0.0024	± 0.0029
$70 < M_{ee} < 78$	± 0.0243	± 0.0037	± 0.0059
$78 < M_{ee} < 88$	± 0.0182	± 0.0033	± 0.0077
$88 < M_{ee} < 94$	± 0.0031	± 0.0017	± 0.0017
$94 < M_{ee} < 105$	± 0.0070	± 0.0044	± 0.0044
$105 < M_{ee} < 120$	± 0.0028	± 0.0106	± 0.0039
$120 < M_{ee} < 140$	± 0.0018	± 0.0019	± 0.0018
$140 < M_{ee} < 200$	± 0.0015	± 0.0038	± 0.0020
$200 < M_{ee} < 300$	± 0.0021	± 0.0044	± 0.0021
$300 < M_{ee} < 400$	± 0.0051	± 0.0065	± 0.0047

TABLE VII: Systematic error in unfolding correction β due to the uncertainty in the electron-photon merging parameter. Errors are shown separately for forward, backward, and all events.

Mass Region (GeV/c^2)	σ_F^{sys}	σ_B^{sys}	σ_{ALL}^{sys}
$50 < M_{ee} < 60$	$^{+0.00014}_{-0.00001}$	$^{+0.00009}_{-0.000002}$	$^{+0.00008}_{-0.000001}$
$60 < M_{ee} < 70$	$^{+0.00253}_{-0.00004}$	$^{+0.00009}_{-0.00014}$	$^{+0.00022}_{-0.00003}$
$70 < M_{ee} < 78$	$^{+0.00100}_{-0.01136}$	$^{+0.00149}_{-0.00056}$	$^{+0.00036}_{-0.00119}$
$78 < M_{ee} < 88$	$^{+0.00418}_{-0.00001}$	$^{+0.00022}_{-0.00092}$	$^{+0.00052}_{-0.00006}$
$88 < M_{ee} < 94$	$^{+0.00001}_{-0.00007}$	$^{+0.00003}_{-0.00002}$	$^{+0.000005}_{-0.00003}$
$94 < M_{ee} < 105$	$^{+0.00188}_{-0.00028}$	$^{+0.00055}_{-0.00483}$	$^{+0.00073}_{-0.00046}$
$105 < M_{ee} < 120$	$^{+0.00355}_{-0.00004}$	$^{+0.01461}_{-0.00067}$	$^{+0.00506}_{-0.00001}$
$120 < M_{ee} < 140$	$^{+0.000004}_{-0.00043}$	$^{+0.00013}_{-0.00087}$	$^{+0.00000}_{-0.00049}$
$140 < M_{ee} < 200$	$^{+0.00008}_{-0.00007}$	$^{+0.00110}_{-0.00027}$	$^{+0.00009}_{-0.00006}$
$200 < M_{ee} < 300$	$^{+0.00012}_{-0.00004}$	$^{+0.00127}_{-0.00004}$	$^{+0.00020}_{-0.00001}$
$300 < M_{ee} < 400$	$^{+0.00001}_{-0.00098}$	$^{+0.00226}_{-0.00065}$	$^{+0.00005}_{-0.00069}$

TABLE VIII: Systematic error in unfolding correction β due to the PDF uncertainty. Errors are shown separately for forward, backward, and all events.

Mass Region (GeV/c^2)	σ_F^{sys}	σ_B^{sys}	σ_{ALL}^{sys}
$50 < M_{ee} < 60$	± 0.0064	± 0.0019	± 0.0033
$60 < M_{ee} < 70$	± 0.0057	± 0.0014	± 0.0019
$70 < M_{ee} < 78$	± 0.0018	± 0.0021	± 0.0018
$78 < M_{ee} < 88$	± 0.0063	± 0.0028	± 0.0008
$88 < M_{ee} < 94$	± 0.0012	± 0.0005	± 0.0007
$94 < M_{ee} < 105$	± 0.0028	± 0.0085	± 0.0008
$105 < M_{ee} < 120$	± 0.0088	± 0.0010	± 0.0072
$120 < M_{ee} < 140$	± 0.0025	± 0.0039	± 0.0021
$140 < M_{ee} < 200$	± 0.0006	± 0.0028	± 0.0007
$200 < M_{ee} < 300$	± 0.0020	± 0.0034	± 0.0022
$300 < M_{ee} < 400$	± 0.0052	± 0.0072	± 0.0054

TABLE IX: Systematic error in unfolding correction β due to uncertainty in the $p_T(e^+e^-)$ distribution. Errors are shown separately for forward, backward, and all events.

X. DRELL-YAN DIFFERENTIAL CROSS SECTION

The differential cross section is calculated by correcting the background-subtracted signal in each M_{ee} bin by the efficiency, unfolding correction, and integrated luminosity:

$$\frac{d\sigma}{dM} = \frac{N - B}{\epsilon\beta\mathcal{L}\Delta M}, \tag{26}$$

where

N = number of observed events in bin i

B = estimate of background in bin i

ϵ = total event selection efficiency (trigger, EM-id, and track match) in bin i

β = unfolding correction factor for acceptance, detector resolution, and QED radiative corrections in bin i

$\mathcal{L}$ = integrated luminosity

ΔM = bin width

The combined efficiency is given by

$$\epsilon_{tot} \;=\; \epsilon_{trig}^{CC-CC} \cdot \epsilon_{EM}^{CC} \cdot \epsilon_{EM}^{CC} \cdot (1 - (1 - \epsilon_{trk}^{CC})^2). \tag{27}$$

The resulting differential cross section $d\sigma/dM$ is shown in Fig. 38. The data are compared with the average theoretical cross section in each bin, obtained from the calulation of Ref. [13] suing the CTEQ6 parton distribution functions. Table X summarizes the input values used to calculate the differential cross section. A breakdown of the systematic errors is given in Table XI.

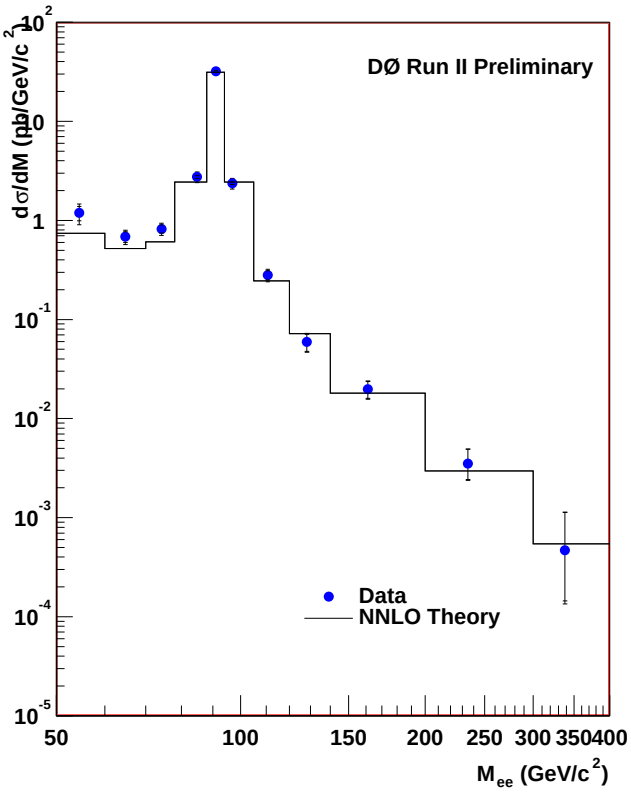

FIG. 38: The Drell-Yan differential cross section. The circles are the data with the error bars representing the total uncertainty (outer error bars) and the statistical uncertainty only (inner error bars). The black line is a NNLO Theoretical calculation [13].

Source	Value	Statistical Error	Systematic Error
Number of Events	5453	74	
Background	136.7	8.0	
PMCS Parameters			
- Scale CC	1.006	0.003	per M_{ee} bin
- Offset CC	0.064	0.045	per M_{ee} bin
- Constant CC	0.045	0.002	per M_{ee} bin
Fake Rate CC	0.016	0.0001	0.002 $(*)$
Trigger Eff. CC-CC	1.0000	$^{+0.0000}_{-0.0002}$	$^{+0.0000}_{-0.0006}$ $(*)$
EM-id Eff. CC	per M_{ee} bin	per M_{ee} bin	per M_{ee} bin
Track Match Eff. CC	per M_{ee} bin	per M_{ee} bin	per M_{ee} bin
Charge Misid Prob. CC	per M_{ee} bin	per M_{ee} bin	per M_{ee} bin
Luminosity	177.3	11.5	
PDF			per M_{ee} bin

TABLE X: Values used in the calculation of the cross section. $(*)$ are systematic errors taken from [14].

Mass Region (GeV/c^2)	σ_{bkgd}	σ_ϵ	σ_β	σ_{PDF}
50 − 60	0.072850	$^{+0.095686}_{-0.127034}$	0.122226	$^{+0.002896}_{-0.000046}$
60 − 70	0.031769	$^{+0.032423}_{-0.037342}$	0.038404	$^{+0.001506}_{-0.000178}$
70 − 78	0.018987	$^{+0.034474}_{-0.038462}$	0.057363	$^{+0.001850}_{-0.006075}$
78 − 88	0.007963	$^{+0.052220}_{-0.053753}$	0.268493	$^{+0.005497}_{-0.000633}$
88 − 94	0.023673	$^{+0.482433}_{-0.485992}$	1.241734	$^{+0.001647}_{-0.009952}$
94 − 105	0.003442	$^{+0.039417}_{-0.040043}$	0.241762	$^{+0.004791}_{-0.003007}$
105 − 120	0.005234	$^{+0.010164}_{-0.011586}$	0.018028	$^{+0.008325}_{-0.000008}$
120 − 140	0.002951	$^{+0.001154}_{-0.001224}$	0.001734	$^{+0.000000}_{-0.000168}$
140 − 200	0.001003	$^{+0.000338}_{-0.000346}$	0.000429	$^{+0.000009}_{-0.000007}$
200 − 300	0.000234	$^{+0.000057}_{-0.000058}$	0.000082	$^{+0.000003}_{-0.000000}$
300 − 400	0.000073	$^{+0.000009}_{-0.000009}$	0.000017	$^{+0.000000}_{-0.000001}$

TABLE XI: Contributions to the systematic error on the differential cross section measurement from uncertainties in the background (σ_{bkgd}), signal selection efficiency (σ_ϵ), unfolding correction (σ_β), and parton distribution functions (σ_{PDF}. Units are pb/(GeV/c^2).

The differential cross sections for forward and backward events are calculated using the same methodology as above, but for events in which the electron angle satisfies cos $\theta^* > 0$ and cos $\theta^* < 0$, respectively. For events with only one track match, the EM candidate with a track match is used to determine the charge. A negative charge indicates an electron, while if the charge is positive the other EM object in the event is assumed to be the electron. Figures 39 and 40 show the forward and backward differential Drell-Yan cross sections $d\sigma_F/dM$ and $d\sigma_B/dM$, respectively. A breakdown of the systematic errors is given in Tables XII-XIII. The results for the differential cross sections are summarized in Tables XIV - XVI.

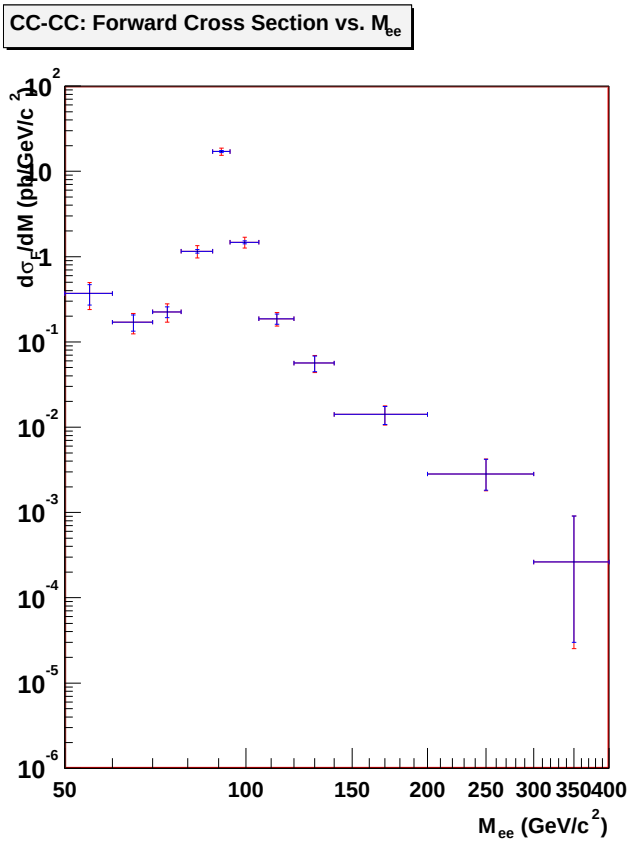

FIG. 39: Forward Drell-Yan differential cross section. The error bars represent the total uncertainty (outer error bars) and the statistical uncertainty only (inner error bars).

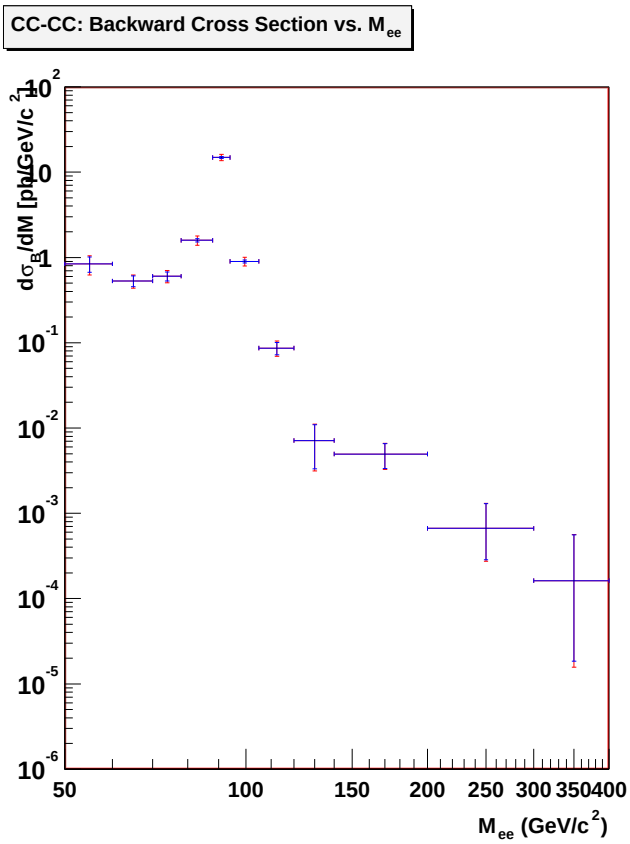

FIG. 40: Backward Drell-Yan differential cross section. The error bars represent the total uncertainty (outer error bars) and the statistical uncertainty only (inner error bars).

Mass Region (GeV/c^2)	σ_{bkgd}	σ_ϵ	σ_β	σ_{PDF}
50 − 60	0.028877	$^{+0.029764}_{-0.039516}$	0.062872	$^{+0.001198}_{-0.000128}$
60 − 70	0.011398	$^{+0.008075}_{-0.009300}$	0.020797	$^{+0.003052}_{-0.000043}$
70 − 78	0.006134	$^{+0.009459}_{-0.010553}$	0.038677	$^{+0.000910}_{-0.010297}$
78 − 88	0.003525	$^{+0.021981}_{-0.022627}$	0.164388	$^{+0.016399}_{-0.000027}$
88 − 94	0.012104	$^{+0.257892}_{-0.259795}$	1.109641	$^{+0.001406}_{-0.014299}$
94 − 105	0.001997	$^{+0.024510}_{-0.024900}$	0.175097	$^{+0.008901}_{-0.001320}$
105 − 120	0.003034	$^{+0.006771}_{-0.007718}$	0.015754	$^{+0.004501}_{-0.000056}$
120 − 140	0.001706	$^{+0.001096}_{-0.001162}$	0.001803	$^{+0.000002}_{-0.000161}$
140 − 200	0.000574	$^{+0.000240}_{-0.000246}$	0.000324	$^{+0.000007}_{-0.000006}$
200 − 300	0.000133	$^{+0.000046}_{-0.000047}$	0.000068	$^{+0.000002}_{-0.000001}$
300 − 400	0.000041	$^{+0.000005}_{-0.000005}$	0.000011	$^{+0.000000}_{-0.000001}$

TABLE XII: Contributions to the systematic error on the forward differential cross section measurement from uncertainties in the background (σ_{bkgd}), signal selection efficiency (σ_ϵ), unfolding correction (σ_β), and parton distribution functions (σ_{PDF}). Units are pb/(GeV/c^2).

Mass Region (GeV/c^2)	σ_{bkgd}	σ_ϵ	σ_β	σ_{PDF}
50 − 60	0.042555	$^{+0.067667}_{-0.089835}$	0.068255	$^{+0.002602}_{-0.000050}$
60 − 70	0.018880	$^{+0.025090}_{-0.028897}$	0.022536	$^{+0.000527}_{-0.000855}$
70 − 78	0.012196	$^{+0.025353}_{-0.028286}$	0.047776	$^{+0.007182}_{-0.002697}$
78 − 88	0.004424	$^{+0.030267}_{-0.031156}$	0.149201	$^{+0.001497}_{-0.006237}$
88 − 94	0.011659	$^{+0.225322}_{-0.226985}$	0.616705	$^{+0.005328}_{-0.003754}$
94 − 105	0.001420	$^{+0.014979}_{-0.015217}$	0.080769	$^{+0.001140}_{-0.009935}$
105 − 120	0.001910	$^{+0.003132}_{-0.003570}$	0.007317	$^{+0.005392}_{-0.000245}$
120 − 140	0.001008	$^{+0.000138}_{-0.000147}$	0.000355	$^{+0.000004}_{-0.000024}$
140 − 200	0.000333	$^{+0.000084}_{-0.000086}$	0.000169	$^{+0.000019}_{-0.000005}$
200 − 300	0.000078	$^{+0.000011}_{-0.000011}$	0.000021	$^{+0.000002}_{-0.000000}$
300 − 400	0.000025	$^{+0.000003}_{-0.000003}$	0.000007	$^{+0.000001}_{-0.000000}$

TABLE XIII: Contributions to the systematic error on the backward differential cross section measurement from uncertainties in the background (σ_{bkgd}), signal selection efficiency (σ_ϵ), unfolding correction (σ_β), and parton distribution functions (σ_{PDF}). Units are pb/(GeV/c^2).

Mass Bin (GeV/c^2)	$\overline{M_{ee}}$ (GeV/c^2)	N	B	$\epsilon\beta$	$d\sigma_{ee}/dM$ (pb / GeV/c^2)
50 − 60	54.5	71	19.7	0.024	$1.1891 \pm 0.1952(\mathrm{stat.})\ ^{+0.1715}_{-0.1907}(\mathrm{sys.})\ ^{+0.0029}_{-0.0000}(\mathrm{pdf})$
60 − 70	63.6	123	31.2	0.076	$0.6840 \pm 0.0826(\mathrm{stat.})\ ^{+0.0595}_{-0.0623}(\mathrm{sys.})\ ^{+0.0015}_{-0.0002}(\mathrm{pdf})$
70 − 78	74.6	154	21.1	0.114	$0.8209 \pm 0.0766(\mathrm{stat.})\ ^{+0.0696}_{-0.0716}(\mathrm{sys.})\ ^{+0.0018}_{-0.0061}(\mathrm{pdf})$
78 − 88	84.5	1022	19.5	0.206	$2.7468 \pm 0.0876(\mathrm{stat.})\ ^{+0.2736}_{-0.2739}(\mathrm{sys.})\ ^{+0.0055}_{-0.0006}(\mathrm{pdf})$
88 − 94	89.9, 92.5	2522	9.2	0.074	$31.9070 \pm 0.6377(\mathrm{stat.})\ ^{+1.3324}_{-1.3337}(\mathrm{sys.})\ ^{+0.0016}_{-0.0100}(\mathrm{pdf})$
94 − 105	97.4	1363	11.1	0.293	$2.3683 \pm 0.0647(\mathrm{stat.})\ ^{+0.2450}_{-0.2451}(\mathrm{sys.})\ ^{+0.0048}_{-0.0030}(\mathrm{pdf})$
Mass Bin (GeV/c^2)	$\overline{M_{ee}}$ (GeV/c^2)	N	B	$\epsilon\beta$	$d\sigma_{ee}/dM$ (fb / GeV/c^2)
105 − 120	111.1	107	9.1	0.131	$280.55 \pm 29.65((\mathrm{stat.})\ ^{+21.35}_{-22.06}(\mathrm{sys.})\ ^{+8.32}_{-0.01}(\mathrm{pdf})$
120 − 140	128.7	37	6.1	0.146	$59.48 \pm 11.71(\mathrm{stat.})\ ^{+3.61}_{-3.63}(\mathrm{sys.})\ ^{+0.00}_{-0.17}(\mathrm{pdf})$
140 − 200	164.1	39	6.5	0.154	$19.87 \pm 3.82(\mathrm{stat.})\ ^{+1.14}_{-1.14}(\mathrm{sys.})\ ^{+0.01}_{-0.01}(\mathrm{pdf})$
200 − 300	240.7	13	1.3	0.188	$3.50^{+1.41}_{-1.07}(\mathrm{stat.})\ ^{+0.25}_{-0.25}(\mathrm{sys.})\ ^{+0.00}_{-0.00}(\mathrm{pdf})$
300 − 400	343.3	2	0.1	0.225	$0.47\ ^{+0.66}_{-0.32}(\mathrm{stat.})\ ^{+0.08}_{-0.08}(\mathrm{sys.})\ ^{+0.00}_{-0.00}(\mathrm{pdf})$

TABLE XIV: Results for the Drell-Yan differential cross section $d\sigma_{ee}/dM$. N is the number of data events, B is the background estimate, and $\epsilon\beta$ is the combined efficiency times unfolding correction. There is an overall fractional uncertainty of 6.5% from the uncertainty in the integrated luminosity. $\overline{M_{ee}}$ is the value of M_{ee} for which the differeantial cross section is equal to its average value over the bin as determined from the theoretical prediction.

Mass Bin (GeV/c^2)	$\overline{M_{ee}}$ (GeV/c^2)	N	B	$\epsilon\beta$	$d\sigma^F_{ee}/dM$ (pb / GeV/c^2)
50 − 60	54.5	30	9.8	0.031	$0.3699 \pm 0.1004(\mathrm{stat.})\ ^{+0.0753}_{-0.0797}(\mathrm{sys.})\ ^{+0.0012}_{-0.0001}(\mathrm{pdf})$
60 − 70	63.6	48	15.6	0.106	$0.1703 \pm 0.0368(\mathrm{stat.})\ ^{+0.0251}_{-0.0255}(\mathrm{sys.})\ ^{+0.0031}_{-0.0000}(\mathrm{pdf})$
70 − 78	74.6	67	10.5	0.177	$0.2252 \pm 0.0326(\mathrm{stat.})\ ^{+0.0403}_{-0.0406}(\mathrm{sys.})\ ^{+0.0009}_{-0.0103}(\mathrm{pdf})$
78 − 88	84.5	487	9.7	0.233	$1.1563 \pm 0.0535(\mathrm{stat.})\ ^{+0.1659}_{-0.1660}(\mathrm{sys.})\ ^{+0.0164}_{-0.0000}(\mathrm{pdf})$
88 − 94	92.5	1321	4.6	0.073	$17.0564 \pm 0.4710(\mathrm{stat.})\ ^{+1.1393}_{-1.1397}(\mathrm{sys.})\ ^{+0.0014}_{-0.0143}(\mathrm{pdf})$
94 − 105	97.4	732	5.5	0.253	$1.4726 \pm 0.0548(\mathrm{stat.})\ ^{+0.1768}_{-0.1769}(\mathrm{sys.})\ ^{+0.0089}_{-0.0013}(\mathrm{pdf})$
Mass Bin (GeV/c^2)	$\overline{M_{ee}}$ (GeV/c^2)	N	B	$\epsilon\beta$	$d\sigma^F_{ee}/dM$ (fb / GeV/c^2)
105 − 120	111.1	61	4.6	0.114	$186.90 \pm 25.86(\mathrm{stat.})\ ^{+17.41}_{-17.80}(\mathrm{sys.})\ ^{+4.50}_{-0.06}(\mathrm{pdf})$
120 − 140	128.7	29	3.1	0.127	$56.48 \pm 11.85(\mathrm{stat.})\ ^{+2.71}_{-2.74}(\mathrm{sys.})\ ^{+0.00}_{-0.16}(\mathrm{pdf})$
140 − 200	164.1	24	3.2	0.135	$14.13\ ^{+3.38}_{-3.38}(\mathrm{stat.})\ ^{+0.70}_{-0.70}(\mathrm{sys.})\ ^{+0.01}_{-0.01}(\mathrm{pdf})$
200 − 300	240.7	9	0.7	0.166	$2.83\ ^{+1.39}_{-1.00}(\mathrm{stat.})\ ^{+0.16}_{-0.16}(\mathrm{sys.})\ ^{+0.00}_{-0.00}(\mathrm{pdf})$
300 − 400	343.3	1	0.1	0.201	$0.26\ ^{+0.65}_{-0.23}(\mathrm{stat.})\ ^{+0.04}_{-0.04}(\mathrm{sys.})\ ^{+0.00}_{-0.00}(\mathrm{pdf})$

TABLE XV: Results for the forward Drell-Yan differential cross section $d\sigma^F_{ee}/dM$. N is the number of data events, B is the background estimate, and $\epsilon\beta$ is the combined efficiency times unfolding correction. There is an overall fractional uncertainty of 6.5% from the uncertainty in the integrated luminosity. $\overline{M_{ee}}$ is the value of M_{ee} for which the differeantial cross section is equal to its average value over the bin as determined from the theoretical prediction.

Mass Bin (GeV/c^2)	$\overline{M_{ee}}$ (GeV/c^2)	N	B	$\epsilon\beta$	$d\sigma^B_{ee}/dM$ (pb / GeV/c^2)
50 − 60	54.5	41	9.8	0.021	$0.8409 \pm 0.1728(\mathrm{stat.})\ ^{+0.1051}_{-0.1206}(\mathrm{sys.})\ ^{+0.0026}_{-0.0000}(\mathrm{pdf})$
60 − 70	63.6	76	15.6	0.064	$0.5293 \pm 0.0768(\mathrm{stat.})\ ^{+0.0387}_{-0.0412}(\mathrm{sys.})\ ^{+0.0005}_{-0.0009}(\mathrm{pdf})$
70 − 78	74.6	87	10.6	0.089	$0.6037 \pm 0.0737(\mathrm{stat.})\ ^{+0.0554}_{-0.0568}(\mathrm{sys.})\ ^{+0.0072}_{-0.0027}(\mathrm{pdf})$
78 − 88	84.5	535	9.8	0.186	$1.5921 \pm 0.0701(\mathrm{stat.})\ ^{+0.1523}_{-0.1525}(\mathrm{sys.})\ ^{+0.0015}_{-0.0062}(\mathrm{pdf})$
88 − 94	92.5	1202	4.6	0.076	$14.9023 \pm 0.4316(\mathrm{stat.})\ ^{+0.6567}_{-0.6573}(\mathrm{sys.})\ ^{+0.0053}_{-0.0038}(\mathrm{pdf})$
94 − 105	97.4	631	5.6	0.356	$0.9000 \pm 0.0361(\mathrm{stat.})\ ^{+0.0822}_{-0.0822}(\mathrm{sys.})\ ^{+0.0011}_{-0.0099}(\mathrm{pdf})$
Mass Bin (GeV/c^2)	$\overline{M_{ee}}$ (GeV/c^2)	N	B	$\epsilon\beta$	$d\sigma^B_{ee}/dM$ (fb / GeV/c^2)
105 − 120	111.1	46	4.6	0.180	$86.45 \pm 14.15(\mathrm{stat.})\ ^{+8.19}_{-8.36}(\mathrm{sys.})\ ^{+5.39}_{-0.25}(\mathrm{pdf})$
120 − 140	128.7	9	3.1	0.215	$7.14\ ^{+3.82}_{-3.82}(\mathrm{stat.})\ ^{+1.08}_{-1.08}(\mathrm{sys.})\ ^{+0.00}_{-0.02}(\mathrm{pdf})$
140 − 200	164.1	16	3.2	0.233	$4.95\ ^{+1.59}_{-1.59}(\mathrm{stat.})\ ^{+0.38}_{-0.38}(\mathrm{sys.})\ ^{+0.02}_{-0.00}(\mathrm{pdf})$
200 − 300	240.7	4	0.7	0.283	$0.67\ ^{+0.63}_{-0.38}(\mathrm{stat.})\ ^{+0.08}_{-0.08}(\mathrm{sys.})\ ^{+0.00}_{-0.00}(\mathrm{pdf})$
300 − 400	343.3	1	0.1	0.325	$0.16\ ^{+0.40}_{-0.14}(\mathrm{stat.})\ ^{+0.03}_{-0.03}(\mathrm{sys.})\ ^{+0.00}_{-0.00}(\mathrm{pdf})$

TABLE XVI: Results for the backward Drell-Yan differential cross section $d\sigma^B_{ee}/dM$. N is the number of data events, B is the background estimate, and $\epsilon\beta$ is the combined efficiency times unfolding correction. There is an overall fractional uncertainty of 6.5% from the uncertainty in the integrated luminosity. $\overline{M_{ee}}$ is the value of M_{ee} for which the differeantial cross section is equal to its average value over the bin as determined from the theoretical prediction.

XI. FORWARD-BACKWARD ASYMMETRY

A. Charge Mismeasurement Probability

Since the forward-backward asymmetry is dependent on measurement of the charge of the electron, we must account for the probability P_m that the electron charge is mismeasured. The meausred A_{FB} will then be related to the true A_{FB} by a dilution factor $\mathcal{D}$:

$$A_{FB}^{meas} = \mathcal{D} A_{FB}^{true} = \mathcal{D}\left(\frac{\sigma_F - \sigma_B}{\sigma_F + \sigma_B}\right). \tag{28}$$

The error on the corrected A_{FB} is

$$\delta A_{FB}^{true} = \sqrt{\left(\frac{A_{FB}^{meas}}{\mathcal{D}^2}\right)^2 (\delta\mathcal{D})^2 + \left(\frac{1}{\mathcal{D}}\right)^2 (\delta A_{FB}^{meas})^2} \tag{29}$$

where

$$\delta A_{FB}^{meas} = 2\frac{\sqrt{\sigma_B^2 \delta\sigma_F^2 + \sigma_F^2 \delta\sigma_B^2}}{(\sigma_F + \sigma_B)^2} \tag{30}$$

The dilution factor for the CC-CC events is given by

$$\mathcal{D} = 1 - 2P_{m,CC} \tag{31}$$

where $P_{m,CC}$ is the probability that the charge of the electron (positron) is measured mismeasured as positive (negative).

The charge mismeasurement probability is measured by using the same selection cuts as is used for the signal events, except that two track matches are required so that the charge of both EM objects is obtained. The charge mismeasurement probability (P_m) is given by

$$P_m = \frac{1}{2} - \sqrt{\frac{1}{4} - \frac{1}{2}\left(\frac{N_{ss}}{N_{os} + N_{ss}}\right)} \tag{32}$$

$$\approx \frac{1}{2}\frac{N_{ss}}{N_{os}} \quad \text{if } N_{ss} \ll N_{os} \tag{33}$$

where

N_{ss} = total number of same-sign events in the Z-peak region

N_{os} = total number of opposite-sign events in the Z-peak region

The Z-boson peak region is taken to be 86 GeV $< M_{ee} <$ 96 GeV. We find the charge mismeasurement probability for CC electrons to be $P_m = 0.006 \pm 0.001(stat) \pm 0.005(sys)$. The systematic error is determined from the variation in the charge misidentification probability as a function of eta, as shown in Fig. 41.

To determine the charge mismeasurement probability as a function of invariant mass, we have modeled the charge mismeasurement probability using Monte Carlo, then normalized the distribution to data in the Z-peak region. Two methods are used to determine the charge mismeasurement probability in Monte Carlo. In the first method, the reconstructed charge

is cpompared to the the generated charge, while the second method is the same as used in the data. The charge mismeasurement probability versus invariant mass for both methods is shown in Fig. 42. Since the methods are consistent and the match method inheritantly gives more statistics, we choose to use the match method to model the charge mismeasurement probability. We studied the charge mismeasurement probability separately for forward and backward events and found that they were consistent, as shown in Fig. 43. Therefore, we use the overall charge mismeasurement probability for all events. Figure 44 shows the charge mismeasurement probability versus invariant mass, which has been normalized to data.

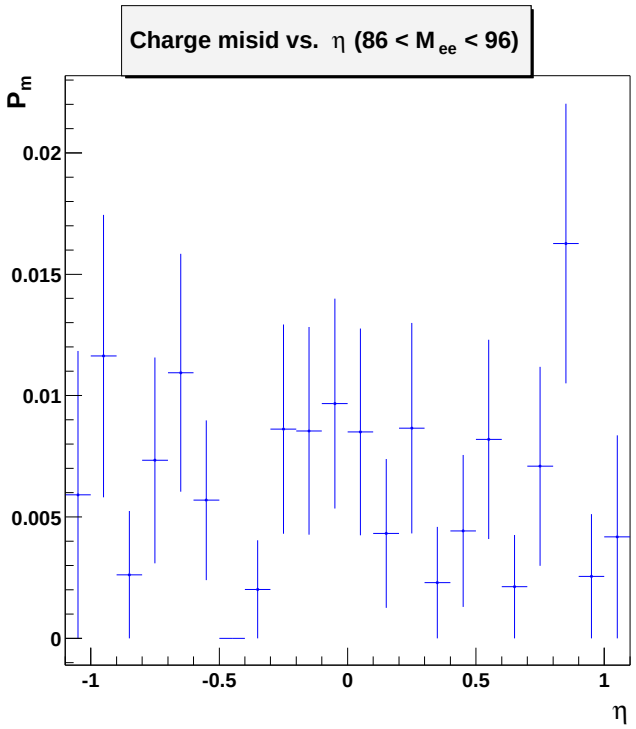

FIG. 41: Charge Misidentification Probability vs. η distribution.

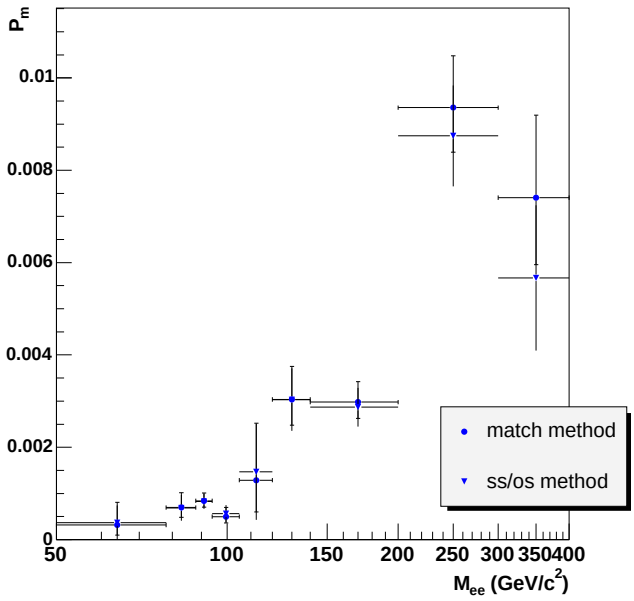

FIG. 42: Charge mismeasurement probability vs. M_{ee} for match method and same-sign/opposite-sign method. The probabilities are not normalized to data.

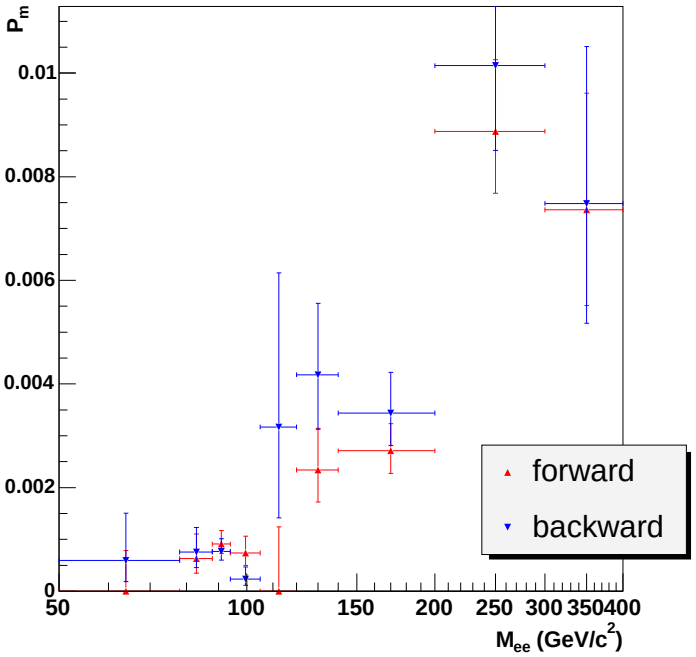

FIG. 43: Charge mismeasurement probability vs. M_{ee} for forward and backward events. The probabilities are not normalized to data.

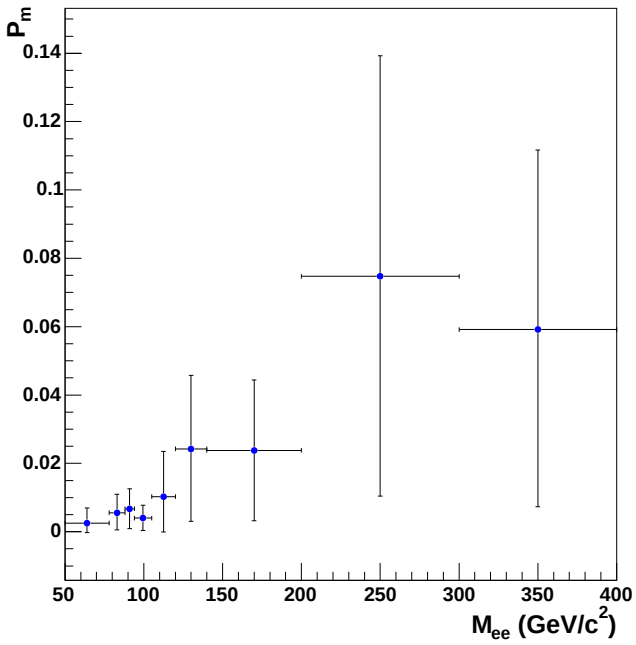

FIG. 44: Charge mismeasurement probability vs. M_{ee} for all events. The probabilities are normalized to data.

B. Forward-Backward Asymmetry Measurement

The results for the forward-backward asymmetry as a function of e^+e^- invariant mass, after correcting for charge mismeasurement, are plotted in Fig. 45. The breakdown of the systematic errors is given in Table XVII and the final results are given in Table XVIII.

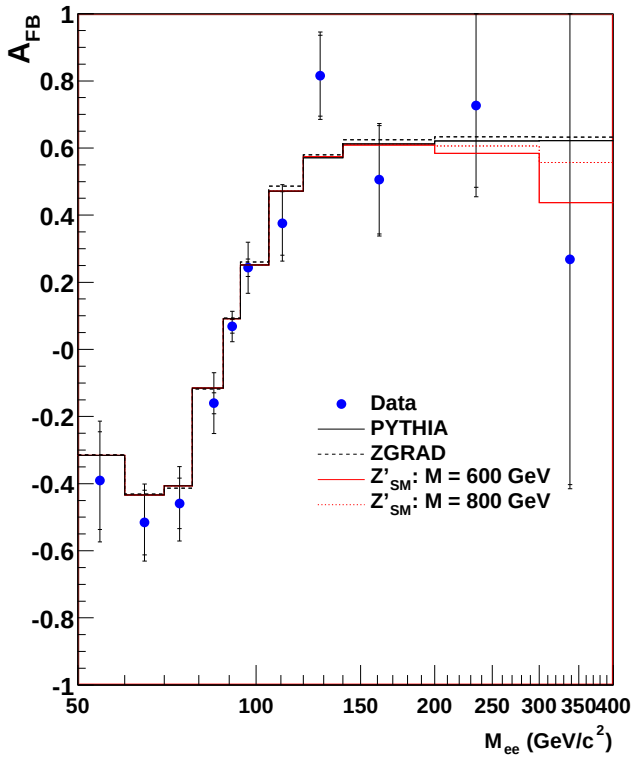

FIG. 45: Forward-backward asymmetry vs. dielectron invariant mass. The blue circles are the data with the error bars representing the total uncertainty (outer error bars) and the statistical uncertainty only (inner error bars). The black histograms are the Born-level theoretical calculation using PYTHIA (solid) and ZGRAD (dashed). The red histograms show the effect of adding a Z' with standard-model couplings to the theoretical prediction, including full $\gamma/Z/Z'$ interference. The predictions are shown for Z' masses of 600 and 800 GeV/c^2. The width of the Z' was assumed to be 0.03 times the Z' mass.

Mass Region (GeV/c^2)	$\sigma_{\mathcal{D}}$	σ_{bkgd}	σ_{ϵ}	σ_{β}	σ_{PDF}
50 − 60	$^{+0.003503}_{-0.002195}$	0.039679	$^{+0.048534}_{-0.064435}$	0.080334	$^{+0.001911}_{-0.000150}$
60 − 70	$^{+0.004621}_{-0.002895}$	0.028076	$^{+0.024821}_{-0.028587}$	0.047874	$^{+0.006644}_{-0.000605}$
70 − 78	$^{+0.004112}_{-0.002576}$	0.013489	$^{+0.023625}_{-0.026359}$	0.075212	$^{+0.004998}_{-0.018273}$
78 − 88	$^{+0.001749}_{-0.001635}$	0.002033	$^{+0.013252}_{-0.013641}$	0.083931	$^{+0.007006}_{-0.001931}$
88 − 94	$^{+0.000815}_{-0.000807}$	0.000533	$^{+0.010788}_{-0.010867}$	0.038898	$^{+0.000185}_{-0.000442}$
94 − 105	$^{+0.001843}_{-0.001750}$	0.000988	$^{+0.011172}_{-0.011350}$	0.070709	$^{+0.002931}_{-0.005257}$
105 − 120	$^{+0.010128}_{-0.007934}$	0.012108	$^{+0.022622}_{-0.025789}$	0.052745	$^{+0.029521}_{-0.001260}$
120 − 140	$^{+0.036822}_{-0.036318}$	0.030251	$^{+0.005744}_{-0.006092}$	0.012369	$^{+0.000107}_{-0.000926}$
140 − 200	$^{+0.021906}_{-0.021792}$	0.031671	$^{+0.009701}_{-0.009939}$	0.016602	$^{+0.001580}_{-0.000424}$
200 − 300	$^{+0.110697}_{-0.109925}$	0.045733	$^{+0.008311}_{-0.008469}$	0.014231	$^{+0.001378}_{-0.000083}$
300 − 400	$^{+0.031940}_{-0.031534}$	0.118337	$^{+0.013837}_{-0.014329}$	0.031868	$^{+0.003037}_{-0.002303}$

TABLE XVII: Contributions to the systematic error on A_{FB} from uncertainties in the dilution factor ($\sigma_{\mathcal{D}}$), background (σ_{bkgd}), signal selection efficiency (σ_{ϵ}), unfolding correction (σ_{β}), and parton distribution functions (σ_{PDF}).

Mass Bin (GeV/c^2)	$\mathcal{D}$	A_{FB}
50 − 60	$0.995\ ^{+0.009}_{-0.006}$	-0.391 ± 0.145(stat.) $^{+0.102}_{-0.110}$(sys.) $^{+0.002}_{-0.000}$(pdf)
60 − 70	$0.995\ ^{+0.009}_{-0.006}$	-0.516 ± 0.096(stat.) $^{+0.061}_{-0.062}$(sys.) $^{+0.007}_{-0.001}$(pdf)
70 − 78	$0.995\ ^{+0.009}_{-0.006}$	-0.459 ± 0.075(stat.) $^{+0.080}_{-0.081}$(sys.) $^{+0.005}_{-0.018}$(pdf)
78 − 88	$0.989\ ^{+0.011}_{-0.010}$	-0.160 ± 0.031(stat.) $^{+0.085}_{-0.085}$(sys.) $^{+0.007}_{-0.002}$(pdf)
88 − 94	$0.987\ ^{+0.012}_{-0.012}$	0.068 ± 0.020(stat.) $^{+0.040}_{-0.040}$(sys.) $^{+0.000}_{-0.000}$(pdf)
94 − 105	$0.992\ ^{+0.008}_{-0.007}$	0.243 ± 0.026(stat.) $^{+0.072}_{-0.072}$(sys.) $^{+0.003}_{-0.005}$(pdf)
105 − 120	$0.979\ ^{+0.026}_{-0.021}$	0.375 ± 0.095(stat.) $^{+0.060}_{-0.060}$(sys.) $^{+0.030}_{-0.001}$(pdf)
120 − 140	$0.952\ ^{+0.043}_{-0.042}$	0.815 ± 0.120(stat.) $^{+0.050}_{-0.049}$(sys.) $^{+0.000}_{-0.001}$(pdf)
140 − 200	$0.952\ ^{+0.041}_{-0.041}$	0.505 ± 0.162(stat.) $^{+0.043}_{-0.043}$(sys.) $^{+0.002}_{-0.000}$(pdf)
200 − 300	$0.951\ ^{+0.129}_{-0.129}$	$0.727\ ^{+0.387}_{-0.244}$(stat.) $^{+0.120}_{-0.120}$(sys.) $^{+0.001}_{-0.000}$(pdf)
300 − 400	$0.882\ ^{+0.105}_{-0.104}$	$0.268\ ^{+1.865}_{-0.671}$(stat.) $^{+0.127}_{-0.127}$(sys.) $^{+0.003}_{-0.002}$(pdf)

TABLE XVIII: The Drell-Yan forward-backward asymmetry results. $\mathcal{D}$ is the dilution factor.

XII. CONCLUSIONS

We have measured the Drell-Yan differential cross section and forward-backward asymmetry in the mass range of 50-400 GeV using a dielectron final state. Results are consistent with the Standard Model expectations.

---

[1] Drell and Yan, Phys. Rev. Lett. **25**, 316 (1970).

[2] J.C. Collins and D.E. Soper, Phys. Rev. **D16**, 2219 (1977).

[3] F. Del Aguila, M. Quirós and F. Zwirner, Nucl. Phys. B **287**, 419 (1987);
J. L. Rosner, Phys. Rev. D **35**, 2244 (1987);
J. L. Rosner, Phys. Rev. D **54**, 1078 (1996).

[4] J. L. Hewett, Phys. Rev. Lett. **82**, 4765 (1999).

[5] T. Sjöstrand, P. Eden, C. Friberg, L. Lonnblad, G. Miu, S. Mrenna, and E. Norrbin, Computer Physics Commun. **135**, 238 (2001).

[6] E. Barbiero and Z. Was, Comput. Phys. Commun. **79** 291 (1994);
E. Barbiero, B. van Eijk, and Z. Was, ibid. **66**, 115 (1991).

[7] J. Zhu, DØ Note 4323, (2004).

[8] J. Pumplin, D.R. Stump, J. Huston, H.L. Lai, P. Nadolsky, and W.K. Tung, J. High Energy Phys. JHEP07, 012 (2002).

[9] U. Yang and Y. Kim, "ISR Studies on Drell-Yan", Fermilab MC Workshop (2003), `http://cepa.fnal.gov/patriot/mc4run2/MCTuning/031204/unki.pdf`

[10] B. Tiller and T. Nunnemann, DØ Note 4660, (2004).

[11] M. Paterno,"Calculating Efficiencies and their Uncertainties", FERMILAB-TM-2286-CD (2004).

[12] G. Gómez, "Extraction of the Width of the W Boson from a Measurement of the Ratio of the W and Z Cross Sections", DØ Ph.D Thesis (1999).

[13] R. Hamberg, W.L. van Neerven, and T. Matsuura, Nucl. Phys. B **359**, 343 (1991);
W. L. Van Neerven and E. B. Zijlstra, Nucl. Phys. B **382**, 11 (1992).

[14] D. Chapin et. al., "Measurement of $Z \to e^+e^-$ and $E \to e^{\pm}\nu$ Production Cross Sections with $|\eta| < 2.3$", DØ Note 4403, Version 1.0 (2004).

[15] U. Baur, S. Keller and W.K. Sakumoto, Phys. Rev. D **57**, 199 (1998).

[16] U. Baur, O. Brein, W. Hollik, C. Schappacher, D. Wackeroth, Phys. Rev. D **65**, 033007 (2002).